

5 Efficient methods for particle-resolved direct numerical simulation*

Markus Uhlmann¹, Jos Derksen², Anthony Wachs^{3,4}, Lian-Ping Wang⁵, Manuel Moriche¹

¹ Karlsruhe Institute of Technology, Institute for Hydromechanics, Kaiserstr. 12, 76131 Karlsruhe, Germany

² University of Aberdeen, School of Engineering, King's College, Aberdeen AB24 3UE, United Kingdom

³ University of British Columbia, Department of Mathematics, 1984 Mathematics Road, Vancouver BC V6T 1Z2, Canada

⁴ University of British Columbia, Department of Chemical and Biological Engineering, 2360 East Mall, Vancouver BC V6T 1Z3, Canada

⁵ Southern University of Science and Technology, Department of Mechanics and Aerospace Engineering, Shenzhen, Guangdong, China

Abstract: In the present chapter we focus on the fundamentals of non-grid-conforming numerical approaches to simulating particulate flows, implementation issues and grid convergence vs. available reference data. The main idea is to avoid adapting the mesh (and – as much as possible – the discrete operators) to the time-dependent fluid domain with the aim to maximize computational efficiency. We restrict our attention to spherical particle shapes (while deviations from sphericity are treated in a subsequent chapter). We show that similar ideas can be successfully implemented in a variety of underlying fluid flow solvers, leading to powerful tools for the direct numerical simulation of large particulate systems.

5.1 Introduction

Particle-resolved direct numerical simulation (PR-DNS) involves the accurate solution of the Navier-Stokes equations for all relevant flow scales in the presence of immersed, moving particles. This includes both: the entire range of the a priori existing turbulent flow features, as well as the details of the disturbance flows induced by the particles. Despite its formidable computational complexity, the PR-DNS approach is now firmly established as a high-fidelity data source which can serve as an alternative or as a complement to laboratory experiments. Since the first pioneering studies of this type which have emerged in the late 1990s, the spectrum of flow classes and added physics which can be tackled with PR-DNS has continuously broadened, and the range of scales that can be faithfully described has grown steadily. This development is owed to the continuing increase in

*Published as Chapter 5 in *Modeling Approaches and Computational Methods for Particle-laden Turbulent Flows*, S. Subramaniam and S. Balachandar (editors), Academic press, 2022, <https://doi.org/10.1016/B978-0-32-390133-8.00013-X>.

available computing capacity coupled with advances in the efficiency of the underlying numerical methods. While very early studies were limited to a small number of particles (e.g. Pan & Banerjee [63] tracked up to 160 moving particles in turbulent channel flow), it is nowadays feasible to describe $O(10^6)$ particles with resources available at many HPC centers [44]. An overview of the physical results which have been extracted from PR-DNS studies to date is given in chapter 6 of the present volume.

In the context of mesh-based numerical methods, there exist two general paradigms for simulating the flow around moving solid objects: boundary-conforming and non-conforming methods. In the former case, the grid is adapted to the time-dependent position of the fluid-solid interface [36, 41]. This requires frequent remeshing steps as well as the corresponding mapping of field quantities to the updated grid, both of which entail a relatively high computational cost. A detailed account of the boundary-conforming approach can be found in the recent review by Wachs [103]. In non-boundary-conforming methods, on the other hand, the fluid-solid interface condition is imposed by other means, such as specifically tailored source terms, modification of the discrete operators, or introduction of Lagrange multipliers. At the same time the computational mesh does not need to be adapted over time, which allows for simple data structures and extremely efficient algorithms from single-phase flow to be applied to the particulate flow problem with relatively few modifications. As a consequence, the fixed-grid approach has become the method of choice for PR-DNS.

In the present chapter we are reviewing several fixed-grid methods which have proved highly productive in the context of turbulent particulate flow, namely the immersed boundary method (§ 5.2), distributed Lagrange multiplier methods (§ 5.3), and Boltzmann-equation based mesoscopic methods (§ 5.4). Our focus is to give an overview of those aspects of the numerical approaches which are deemed most relevant to PR-DNS. Due to space restrictions, however, not all methods which today are being successfully used in the community for these types of applications can be covered here. Some notable omissions in this text are listed in the following: sharp interface and cut-cell methods [94, 79], volume penalization [3, 48], overset-grids [11, 35], and coupling to a local Stokes flow solution [121]. Furthermore, a comprehensive comparison of these different methods is not undertaken here, since it would require a significant collaborative effort (cf. discussion in § 5.6). It should also be noted that excellent previous reviews have been published on immersed boundary methods in a general context [59], on immersed boundary methods designed specifically for particulate flow [34], on the immersed boundary method for fluid-structure interaction [86, 47], and on particle-resolved methods for complex-shaped bodies [103].

5.2 The immersed boundary method in Navier-Stokes-based solvers

The immersed boundary method (often abbreviated as IBM) goes back to the work of Peskin [68] (cf. also [69, 70]) who designed it as a means to perform simulations of the flow around heart valves. The valves in the original work are treated as flexible objects which deform and translate under the fluid load, while at the same time exerting a force upon the fluid. In order to achieve this, Lagrangian marker points are attached to the immersed object which are advected with the local fluid velocity; the deformation of the marker point configuration then leads to internal stresses (depending on the desired material properties) which are spread back to the Eulerian grid. This in turn yields an additional force term, henceforth denoted as \mathbf{f} , which appears on the right-hand-side of the fluid momentum equation. Therefore, the following three steps are the key ingredients of an immersed boundary method: (i) interpolation of the velocity field from the Eulerian grid to the Lagrangian marker positions; (ii)

computation of the stresses acting at the Lagrangian points; (iii) spreading of the stresses back to the Eulerian grid. Steps (i) and (iii) are closely related operations which in a continuous formulation involve integrals over Dirac delta functions. For the discrete counterpart Peskin [69] devised regularized delta functions which ensure smooth interpolation and spreading for arbitrarily located force points (cf. also [70]).

Now, when the immersed solid object of interest is not flexible, but a perfectly rigid body, the appropriate material property can be mimicked in the original immersed-boundary context by a spring-like behavior with large stiffness linking neighboring marker points [29, 77]. This feed-back forcing approach, however, has the drawback of presenting severe time step restrictions and of introducing numerical parameters which require some amount of tuning in practice. As a consequence, feed-back forcing is typically avoided in PR-DNS applications.

5.2.1 Direct forcing immersed boundary method

Mohd-Yusof [60] (cf. also [18]) realized that the feed-back procedure can be circumvented by constructing the forcing term such that the “desired” velocity is directly obtained after each time step. The basic idea can be demonstrated by writing the Navier-Stokes momentum equation (1.3) in the following simple semi-discrete form [18]

$$\frac{\mathbf{u}_f^{n+1} - \mathbf{u}_f^n}{\Delta t} = \mathbf{RHS}^{n+1/2} + \mathbf{f}^{n+1/2}, \quad (5.1)$$

where the superscript indicates a discrete time level, \mathbf{RHS} regroups the advective, viscous and pressure terms (which are evaluated at some intermediate time with index $n + 1/2$), and Δt is the discrete time step. Supposing that a desired velocity value $\mathbf{u}_f^{(d)}$ is known at a grid point coinciding with the fluid-solid interface, an explicit expression for the forcing term $\mathbf{f}^{n+1/2}$ can be obtained from (5.1) by requiring that $\mathbf{u}_f^{n+1} = \mathbf{u}_f^{(d)}$, viz. [18]

$$\mathbf{f}^{n+1/2} = \frac{\mathbf{u}_f^{(d)} - \mathbf{u}_f^n}{\Delta t} - \mathbf{RHS}^{n+1/2}. \quad (5.2)$$

Since, however, the particle surface does in general not coincide with the Eulerian grid nodes, interpolation of some kind is necessary in order to define the desired velocity. Various interpolation techniques have been proposed in the past, either based upon (linear) grid-based operations [18, 46], or on a combination of grid-based operations and use of a regularized delta function [53]. In [95] a slightly different approach is taken: a preliminary velocity field is first interpolated to Lagrangian marker locations on the fluid-solid interface (as in Peskin’s original method), then the force term is computed in the spirit of (5.2), and finally the force is transferred back to the Eulerian grid, again using Peskin’s original spreading operator. Since the method presented in [95] serves as a foundation for many subsequent refinements, we will specify it here in more detail.

Let us define a set of N_L Lagrangian marker points distributed over the immersed surface of a solid object, with $\mathbf{X}_k(t)$ denoting the k th marker’s position at time t (cf. figure 5.1). Each Lagrangian marker is associated with a forcing volume ΔV_k which is of the order of a grid cell volume. The first step is to determine a preliminary velocity field $\tilde{\mathbf{u}}_f$, solution of the momentum equation (5.1) in the absence of any immersed-boundary forcing, viz.

$$\frac{\tilde{\mathbf{u}}_f - \mathbf{u}_f^n}{\Delta t} = \mathbf{RHS}^{n+1/2}. \quad (5.3)$$

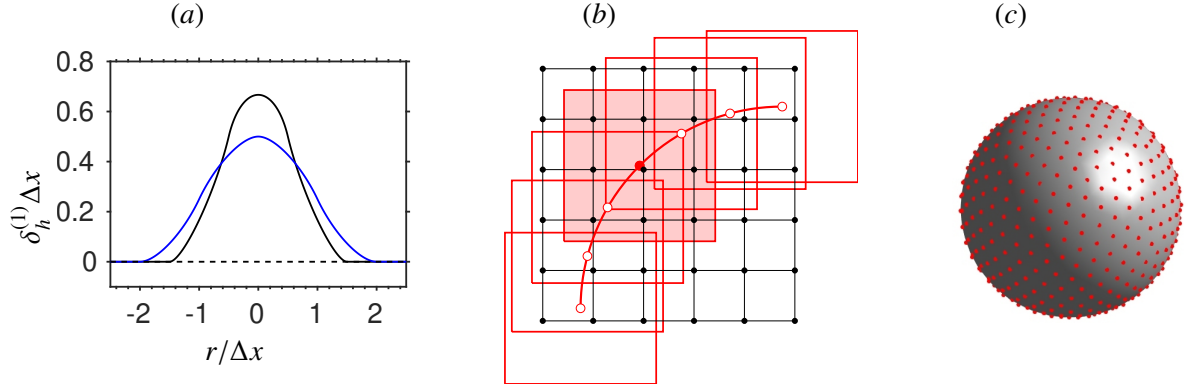


Figure 5.1: (a) Discrete delta function kernel $\delta_h^{(1)}(r)$ used in the interpolation (5.4) and spreading (5.6) of variables between Eulerian and Lagrangian locations: — 3-point function of [75]; — 4-point function of [70]. The three-dimensional kernel is defined as the tensor product of the one-dimensional kernels, viz. $\delta_h(\mathbf{r}) = \delta_h^{(1)}(r_1)\delta_h^{(1)}(r_2)\delta_h^{(1)}(r_3)$. (b) Sketch of a uniform and isotropic Eulerian grid (grid points in black) and of the Lagrangian marker points (red dots) distributed along a segment of a circle. In this case a distribution with an arc-length $\Delta s = \Delta x$ has been chosen. The red squares indicate the support of the discrete delta function kernel (in this case the 3-point function of [75]) associated to each Lagrangian marker point. (c) Distribution of 515 Lagrangian points on the surface of a sphere (as e.g. used in an IBM when $d_p/\Delta x = 13$), obtained via a repulsion force algorithm [76].

Next, the field $\tilde{\mathbf{u}}_f$ is interpolated to the set of Lagrangian marker points with the aid of the regularized delta function δ_h :

$$\tilde{\mathbf{U}}_f(\mathbf{X}_l) = \sum_{i,j,k} \tilde{\mathbf{u}}_f(\mathbf{x}_{ijk}) \delta_h(\mathbf{X}_l - \mathbf{x}_{ijk}) \Delta x^3, \quad \forall l. \quad (5.4)$$

In (5.4) we assume that the Eulerian grid is uniform and isotropic, i.e. that $\mathbf{x}_{ijk} = (i\Delta x, j\Delta x, k\Delta x)$. The specific force \mathbf{F} which drives the preliminary velocity towards the desired value $\mathbf{U}^{(d)}$ at a given Lagrangian marker point (which can be expressed in terms of the particle's translational and rotational velocity) is then obtained through the following relation:

$$\mathbf{F}(\mathbf{X}_l) = \frac{\mathbf{U}^{(d)}(\mathbf{X}_l) - \tilde{\mathbf{U}}_f(\mathbf{X}_l)}{\Delta t}, \quad \forall l. \quad (5.5)$$

Finally, the force at the Lagrangian positions is spread back to the Eulerian grid,

$$\mathbf{f}^{n+1/2}(\mathbf{x}_{ijk}) = \sum_l \mathbf{F}(\mathbf{X}_l) \delta_h(\mathbf{X}_l - \mathbf{x}_{ijk}) \Delta V_l, \quad \forall i, j, k, \quad (5.6)$$

which then lets us solve the momentum equation (5.1) over the entire domain occupied by both fluid and solid phases.

The immersed boundary method as outlined in equations (5.1) and (5.3-5.6) is particularly well adapted to PR-DNS as it allows for smooth variations of hydrodynamic force and torque while particles are free to translate with respect to the Eulerian grid. At the same time the sharp interface is essentially “smeared” over the width of the transfer kernel function, which has a support of three to four grid widths in typical applications. One consequence of “smearing” the fluid-solid interface in diffuse interface methods is that the drag force on a particle tends to be overestimated (cf. § 5.2.3

below for a demonstration with the aid of a scalar equation in one space dimension and further discussion of this issue). Here the regularized delta function as constructed by Peskin [70] guarantees that the net force and torque acting on a body are preserved by the spreading step. This equivalence is, however, limited to uniform Cartesian grid systems; interpolation and spreading operators applicable to non-uniform and curvilinear grids have been proposed by various authors [120, 98, 71, 1]. In practice it is relatively straightforward to implement the algorithm outlined above into different flow solvers with various flavors of temporal and spatial discretizations.

5.2.2 How and where to distribute Lagrangian marker points?

Let us first consider the case where we wish to distribute Lagrangian points over the surface of a sphere. On a uniform grid, a computationally optimal distribution is such that the points are “evenly” spread in some sense, as it should require the smallest total number of points (and hence the lowest operation count) for a desired point density. Although no unique measure of “evenness” of a spatial distribution in three spatial dimensions exists, both iterative approaches as well as explicit constructions on the sphere are available for practical purposes, as discussed e.g. in [76] and [52].

Since the early work of Fadlun et al. [18] many researchers have chosen to apply an immersed boundary force only at the fluid-solid interface, while allowing the flow field in the interior of the solid domain to evolve freely. Although the impact of these parasitic currents upon the flow in the actual fluid domain is generally found to be small, their effect can in some cases become noticeable. Moriche et al. [61] report a case of non-physical path oscillations due to surface forcing in their simulations of mildly oblate spheroids with relatively small excess density settling under gravity. Uhlmann [96] observed that applying the direct forcing immersed-boundary procedure throughout the volume occupied by the solid particle tends to reduce the slip error at the interface for low Reynolds number flows. Therefore, it is sometimes beneficial to collocate Lagrangian force points throughout the solid volume, in the spirit of DLM methods discussed in § 5.3, although this entails an increase in the particle-related operation count. For this purpose additional interior layers of force points can simply be added (akin to an onion) until the particle volume is covered. This construction is not applicable to shapes which deviate strongly from a sphere. In the general case, an iterative (but still relatively efficient) algorithm based on Voronoï tessellation is available [61, appendix B2]. Note that the present discussion equally applies to fluid-solid coupling methods other than of immersed-boundary type (cf. §5.3-5.4).

Let us now turn to the choice for the number of Lagrangian marker points to be distributed at the fluid-solid interface. It is common practice to use a marker density comparable to the density of the Eulerian grid points [95]. It is also intuitively clear that the allowed minimum density is such that the support of the discrete delta function at neighboring marker points just overlaps – otherwise the surface becomes permeable. Zhou & Balachandar [122] have considered the volume ΔV_l in (5.6) as an adjustable weight factor, and their analysis then somewhat surprisingly shows that the optimal choice (from the point of view of efficiency) corresponds to the minimum marker density. This is due to the fact that the amplitude of the velocity error (under the above mentioned condition on overlapping delta functions, and for sufficiently small time steps) does not significantly affect the value of the immersed-boundary force [122]. We will return to this point in § 5.2.4.

5.2.3 What level of accuracy can be achieved with the immersed boundary method?

Beyer & LeVeque [6] have shown for one-dimensional problems with singular source terms that the

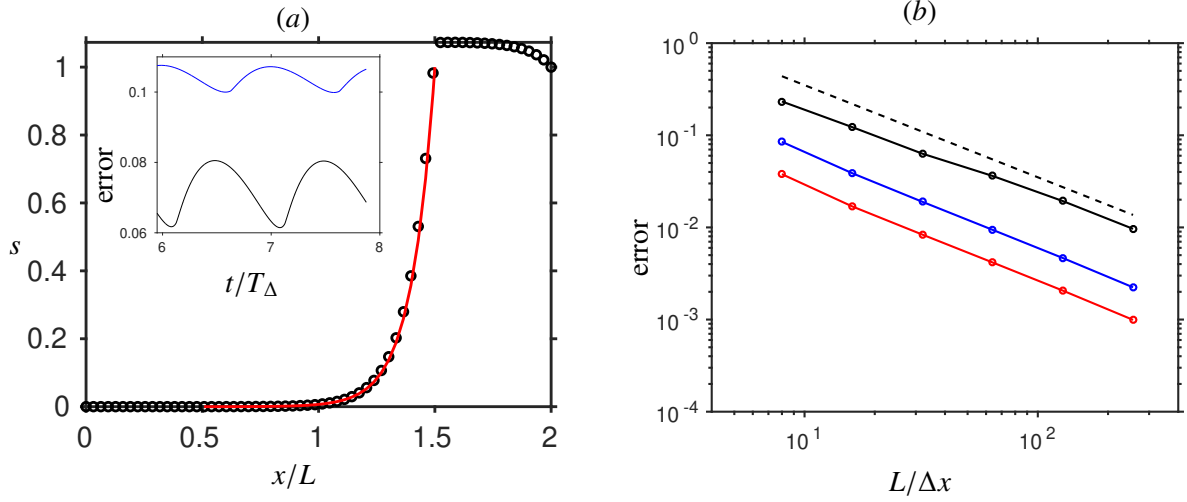


Figure 5.2: Scalar advection-diffusion problem in one space dimension (5.7), computed with the immersed boundary method in a standard second-order finite-difference discretization on a uniform grid and discretized in time with an explicit Euler scheme. (a) Solution for $Pe = 10$, $u_w/u_{adv} = 0.1$ at time $t/T_{adv} = 2.5$ (where $T_{adv} = L/u_{adv}$ and $u_{adv} = c - u_w$), computed with $L_x/L = 2$, $x_1(t=0)/L = 0.25$, $L/\Delta x = 31.5$, $\sigma = c\Delta t/\Delta x = 0.0087$, $\beta = D_s\Delta t/\Delta x^2 = 0.025$. The solid red line corresponds to the exact solution in I_p . The inset shows the relative error of the scalar boundary flux, $D_s s_{,x}(x_2)$, as a function of time, where $T_\Delta = \Delta x/u_w$ is the interval during which the immersed boundary traverses one grid cell (the black curve is for the three-point delta function of [75], the blue curve for the four-point function of [68]). (b) Convergence of the solution under spatial refinement. The lines with symbols indicate different error norms (L_∞ , L_1 , L_2) of the scalar field evaluated on the Eulerian grid points $x_i \in I_p$, while the dashed line is proportional to $\Delta x/L$. The time step was kept constant, such that $\sigma = 0.0011$ and $\beta = 0.025$ on the finest grid.

immersed boundary method with discretized delta functions commonly employed [e.g. 75] is only first-order accurate in space when the error is measured on the Eulerian grid. This convergence result also applies to the force acting on the submerged body, as has been demonstrated by Zhou & Balachandar [122].

Let us consider a simple one-dimensional problem which will illustrate some of the features of the immersed-boundary method. We will solve the advection-diffusion equation for a scalar quantity $s(x, t)$, viz.

$$s_{,t} + c s_{,x} = D_s s_{,xx}, \quad (5.7)$$

where $c > 0$ is the constant advection speed and D_s is the diffusivity. The spatial interval of interest is $I_p = [x_1, x_2]$ with $x_2 = x_1 + L$. The problem with Dirichlet boundary conditions $s(x_1) = s_1$ and $s(x_2) = s_2$ has a steady-state solution

$$s = s_1 + (s_2 - s_1) (\exp(Pe \tilde{x}/L) - 1) / (\exp(Pe) - 1) \quad (5.8)$$

where $Pe = (c - u_w)L/D_s$ is the Peclet number, $u_w = cst$ is the velocity of the immersed boundaries, and $\tilde{x} = x - u_w t$ is the position in a frame of reference moving with u_w . The asymptotic solution, which features an exponential boundary layer that steepens with Pe (figure 5.2a), shall be computed on a fixed grid in the interval $I_c = [0, L_x]$, using the immersed boundary method to enforce the conditions

on s at x_1, x_2 , while imposing the same Dirichlet conditions at the outer domain boundaries (i.e. $s(0) = s_1, s(L_x) = s_2$) in a conventional way. We choose the computational domain such that $0 < x_1$ and $x_2 < L_x$ for the duration of the computation (alternatively, one can also impose periodic outer boundary conditions).

The results summarized in figure 5.2 show that the solution computed with the immersed boundary method is well-behaved, and that it is indeed first-order accurate in space when measured (using different norms) on the Eulerian grid points for which $x_i \in I_p$. The same is true for the scalar boundary flux (equivalent to a Nusselt or Sherwood number, not shown) which would be the typical quantity of interest here. Note that the flux is systematically overestimated, a result which carries over to the drag force when applying the immersed boundary method to the Navier-Stokes equations [cf. the discussion in 122]. For this reason some authors have proposed to retract the Lagrangian force points from the actual particle surface based on empirical corrections [10, 55]. Other authors have proposed immersed boundary schemes which avoid to spread the forcing term into the volume occupied by the fluid phase [92], thereby maintaining the momentum balance untainted. It is also important to note in the present figure 5.2a (inset) that the amplitude of the error varies smoothly while the forcing points (x_1, x_2) are translating across the Eulerian grid. A number of kernel functions for the interpolation (5.4) and spreading (5.6) of quantities between Eulerian and Lagrangian positions have been proposed in the literature, and the reader is referred to [70] for a thorough discussion of the invariance properties and moment conditions which can be achieved. Due to its support of only three grid points in each linear dimension the variant stated in [75] has been widely used for PR-DNS. Discretized delta functions with broader support generally yield smoother signals during grid traverse; however, they typically lead to larger errors in the predicted fluxes (cf. figure 5.2a, inset).

It should be noted that second-order spatial accuracy can be achieved by modifying the finite-difference operators in the vicinity of the immersed boundary [e.g. 56, 58]. These “sharp-interface” or “ghost-cell” methods, however, are significantly more complex from the computational point of view, especially when systems with a large number of mobile particles are considered.

5.2.4 Further refinements

It appears reasonable to ask how well the immersed boundary method manages to impose the desired velocity at the Lagrangian marker points at the end of a given time step. Gsell & Favier [30] have shown that the discrepancy (i.e. the difference between the updated and the desired velocities at the Lagrangian marker points) depends essentially on the reciprocity of the interpolation and spreading operators (5.4,5.6). When considering an isolated Lagrangian force point (such as on either boundary in the one-dimensional equation 5.7), the discrepancy is proportional to the deviation from unity of the sum (over its support) of the square of the discrete delta function. In order to reduce the Lagrangian velocity error, Gsell & Favier [30] propose to multiply the Lagrangian force relation (5.5) by a constant correction factor which only depends on the choice of the kernel function. In the case of an isolated Lagrangian marker point and for a scalar equation, this procedure guarantees that the desired velocity is exactly enforced. In the case of multi-dimensional immersed interfaces (e.g. a sphere), the overlap between the supports of delta functions centered at neighboring Lagrangian points makes this procedure approximate. It should be noted, however, that the reduction (or even elimination) of the velocity error at the Lagrangian marker points does not guarantee a similar reduction of the error at the Eulerian grid points in the fluid domain. In fact, the error shown in figure 5.2(b) remains practically identically when the correction proposed in [30] is applied, and the same is true for the interface flux (not shown). This is consistent with the analysis of Zhou & Balachandar [122] which we have already discussed above. Further investigations involving freely-moving particles should be performed in the

future in order to explore the potential of this approach.

Incidentally, the so-called “multi-direct” forcing approach [54], where the immersed boundary force computation (5.4-5.6) is repeatedly carried out per time step while the force field $\mathbf{f}^{n+1/2}$ is being summed up, can be interpreted as an iterative way of achieving essentially the same effect (in the limit of an infinite number of iterations) as through the explicit correction method of Gsell & Favier [30].

Another point to consider is the consequence of using the immersed boundary method in the context of a fractional step method. In this case the modification introduced by the projection step leads to a discrepancy which typically scales with the time step and with the viscosity. One remedy is, therefore, to employ relatively small time steps. With efficiency in mind, it would be preferable to construct interpolation and spreading kernels which are divergence-free in a discrete sense. Bao et al. [4] have proposed such an ansatz, which, however, requires the solution of additional global Poisson problems at each time step. Alternatively, Taira & Colonius [87] have shown how to absorb an immersed-boundary-like procedure into the projection step of a fractional step method with the aid of an algebraic procedure that is somewhat related to the Lagrange multiplier method (cf. § 5.3). However, it is not clear how their technique can be applied to freely-mobile immersed bodies.

5.2.5 Describing the motion of rigid particles

In the PR-DNS approach the Newton-Euler equations for the motion of rigid bodies (1.5)-(1.6) need to be solved for each particle, with the hydrodynamic force and torque (1.7)-(1.8) being directly obtained from the numerical approximation of the Navier-Stokes equations at sufficient accuracy. Since a direct evaluation of the surface integrals in (1.7)-(1.8) is relatively costly, it is computationally more efficient to express the hydrodynamic force and torque indirectly with the aid of the immersed-boundary forcing term which is already available. More specifically, it can be shown that under the assumption of rigid body motion ($\mathbf{u} = \mathbf{V}_p + \boldsymbol{\Omega}_p \times \mathbf{r}$, where \mathbf{r} is the distance from the center of mass) throughout the volume occupied by the particle we have:

$$\frac{d}{dt} \oint_{\partial V_p^{(i)}} \mathbf{u} dV = V_p \frac{d\mathbf{V}_p^{(i)}}{dt}, \quad (5.9)$$

and analogously for the moment of moments [95]. Note that in the present section it is understood that \mathbf{u} (without any subscript for a phase) refers to the composite velocity field defined throughout the joint volume occupied by either the fluid or the particles. The assumption of rigid body motion inside the volume occupied by the solid, therefore, allows us to express the hydrodynamic force acting on the i th particle as:

$$\mathbf{F}_h^{(i)} = \rho_f V_p \frac{d\mathbf{V}_p^{(i)}}{dt} - \rho_f \sum_{l=1}^{N_L^{(i)}} \mathbf{F}(\mathbf{X}_l^{(i)}) \Delta V_l^{(i)}, \quad (5.10)$$

(where we have added the particle index as super-scripts to the Lagrangian quantities for notational consistency), and again analogously for the torque. Relation (5.10) expresses the fact that the net force arises from the sum of one contribution which is described by the acceleration of the composite fluid (which is treated as a single phase with density ρ_f) and another contribution due to the applied immersed boundary forcing (defined in 5.5). The advantage of using (5.10) is that the hydrodynamic force can be determined at practically no additional cost, which typically makes tracking particles very efficient in the context of immersed boundary methods (except for very dense suspensions, where the cost of treating solid-solid contact becomes significant, cf. chapter 11). On the downside, the use of relation (5.10) leads to a singularity for the density-matched case ($\rho_p = \rho_f$), as the particle acceleration

then drops out of equation (1.5). However, for the time being let us restrict our attention to particles with density larger than the fluid density; the density-matched case and the treatment of light particles will be discussed below.

We are now in a position to put all ingredients together, namely: (i) the method to determine the fluid-solid interface coupling term (equations 5.3-5.6), (ii) the hydrodynamic force (5.10), and the analogous term for the torque, required to advance the particle state variables (position and velocity), (iii) the basic single-phase Navier-Stokes solver. It remains to specify the type of inter-phase coupling to be employed. Weak (or explicit) coupling, where the most recent values of the variables describing the state of one phase are used for the purpose of updating the other phase, is the typical choice for the obvious reason of efficiency. In this case a number of conditions for stable integration arise which depend on the solid-fluid density ratio, on the details of the temporal discretization, on the distribution of the Lagrangian markers, and on the choice of the regularized delta function [122]. In practice, the standard weakly-coupled approach is limited to particles with an excess density (Uhlmann [95] reports stable integration for $\rho_p/\rho_f > 1.2$, while Zhou & Balachandar [122] have shown how this limit can be somewhat lowered by adapting the value of the volume associated with the Lagrangian points).

Patankar [64] has proposed a method which allows to treat the density-matched case ($\rho_p = \rho_f$) by computing the rigid particle velocity through integration of the (computational) velocity field over the particle volume, thereby circumventing the above-mentioned singularity (cf. also [84]) and at the same time obviating the need to explicitly solve the Newton-Euler equations (1.5)-(1.6). Another interesting route has been taken by Kim & Choi [45] who propose to integrate the particle momentum equation with a Crank-Nicolson method (i.e. with implicit coupling), and then show how the evaluation of the hydrodynamic force at the new (unknown) time level can be avoided through use of Lagrangian quantities. As a result, the final formulation is non-iterative and free from a singularity for the density-matched case. Applications of this method to the motion of light particles, however, have not been published to our knowledge. A somewhat different approach is taken by Schwarz et al. [80] who introduce a stabilizing term on both sides of the Newton-Euler equations for rigid particle motion (which is termed ‘virtual mass force’), allowing for small density ratios to be tackled. This technique has subsequently been refined for larger volume fractions [89]. Yet another approach is due to Tschisgale et al. [93] (cf. also [43]), who define an interface layer (with finite thickness) to which the rigid-body assumption is restricted. This then leads to a discrete particle momentum equation which is also free from the above mentioned singularity, and which even remains valid in the limit of vanishing particle mass.

5.3 Distributed Lagrange multiplier methods

The Direct Forcing IB methods presented in § 5.2.1 are powerful numerical methods. However, the forcing term is explicit in time and may create stability issues for low density ratio. The forcing term is also distributed on the particle surface only, hence leaving a non-physical spurious flow inside rigid particles. Implicit variants have been proposed in the form of a fixed-point iteration to compute the forcing term [10, 43] while volume forcing has been recently suggested by [61]. However, the Distributed Lagrange Multiplier/Fictitious Domain, abbreviated DLM/FD in the literature and introduced by Glowinski and co-authors in 1999 [25, 26] naturally features implicit forcing and volume forcing. The foundation of the original DLM/FD method is to derive a global variational formulation for the fluid and particle momentum conservation equations that allows to solve the fluid momentum and

mass conservation in the entire fluid domain through the following symbolic operation:

$$\begin{aligned} \int_{\Omega \setminus \mathcal{P}} (\text{fluid momentum}) \cdot \boldsymbol{v} dx + (\text{particle translational momentum}) \cdot \boldsymbol{V} \\ + (\text{particle angular momentum}) \cdot \boldsymbol{\xi} = \mathbf{0}, \end{aligned} \quad (5.11)$$

where $(\boldsymbol{v}, \boldsymbol{V}, \boldsymbol{\xi})$ are the test functions for $(\boldsymbol{u}, \boldsymbol{U}, \boldsymbol{\omega})$. The fluid mass conservation is easily extended from $\Omega \setminus \mathcal{P}$ to Ω as a rigid body motion is mass conserving by construction. The extension of the fluid momentum conservation equation from $\Omega \setminus \mathcal{P}$ to Ω requires a bit more care and a few rather simple technicalities that the reader can straightforwardly find in [25, 26]. In summary, once extended in the rigid particle region, the fluid is forced to satisfy a rigid body motion through the introduction of distributed Lagrange multipliers over both the particle surface and the particle volume. The resulting set of DLM/FD equations with homogeneous Dirichlet boundary conditions on $\partial\Omega$ (without any loss of generality) written in a variational form reads as follows:

1. Combined momentum equations

$$\int_{\Omega} \rho_f \left(\frac{\partial \boldsymbol{u}}{\partial t} + (\boldsymbol{u} \cdot \nabla) \boldsymbol{u} \right) \cdot \boldsymbol{v} dx - \int_{\Omega} p \nabla \cdot \boldsymbol{v} dx + \int_{\Omega} \mu_f \nabla \boldsymbol{u} : \nabla \boldsymbol{v} dx + \sum_{i=0}^{N-1} \int_{\mathcal{P}_i(t)} \boldsymbol{\lambda} \cdot \boldsymbol{v} dx = \mathbf{0}, \quad (5.12)$$

$$\begin{aligned} \left(1 - \frac{\rho_f}{\rho_p} \right) \left[M_i \left(\frac{d\boldsymbol{U}_i}{dt} - \boldsymbol{g} \right) \cdot \boldsymbol{V}_i + \frac{d\boldsymbol{J}_i \boldsymbol{\omega}_i}{dt} \cdot \boldsymbol{\xi}_i \right] - \sum_j \boldsymbol{F}_{c,ij} \cdot \boldsymbol{V}_i - \sum_w \boldsymbol{F}_{c,iw} \cdot \boldsymbol{V}_i \\ - \sum_j \boldsymbol{F}_{c,ij} \cdot \boldsymbol{\xi}_i \times \boldsymbol{R}_j - \sum_w \boldsymbol{F}_{c,iw} \cdot \boldsymbol{\xi}_i \times \boldsymbol{R}_j - \int_{\mathcal{P}_i(t)} \boldsymbol{\lambda} \cdot (\boldsymbol{V}_i + \boldsymbol{\xi}_i \times \boldsymbol{r}) dx = \mathbf{0}, \quad i = 0, \dots, N-1 \end{aligned} \quad (5.13)$$

$$\int_{\mathcal{P}_i(t)} \boldsymbol{\alpha} \cdot (\boldsymbol{u} - (\boldsymbol{U}_i + \boldsymbol{\omega}_i \times \boldsymbol{r})) dx = 0, \quad i = 0, \dots, N-1. \quad (5.14)$$

2. Continuity equation

$$- \int_{\Omega} q \nabla \cdot \boldsymbol{u} dx = 0. \quad (5.15)$$

where $\boldsymbol{\lambda}$ denotes the distributed Lagrange multiplier vector related to the rigid body constraint $\boldsymbol{u} = \boldsymbol{U} + \boldsymbol{\omega} \times \boldsymbol{r}$, $\boldsymbol{F}_{c,ij}$ and $\boldsymbol{F}_{c,iw}$ denote the particle-particle and particle-wall contact forces, respectively, $(\boldsymbol{\alpha}, \boldsymbol{V})$ are the test functions for $(p, \boldsymbol{\lambda})$, respectively, \boldsymbol{V}_i and $\boldsymbol{\xi}_i$ are simple functions the components of which are uniformly equal to 1 over $\mathcal{P}_i(t)$ and all functions belong to the appropriate functional spaces [25, 26]. The factor $(1 - \rho_f/\rho_p)$ is the result of extending the fluid momentum equation from $\Omega \setminus \mathcal{P}$ to Ω [25]. Note that the formulation breaks down when $\rho_f \leq \rho_p$. i.e., for both neutrally buoyant and lighter particles. This issue can be fixed in various manners: (i) through the derivation of an alternative DLM/FD formulation [65] in which $\boldsymbol{D}(\boldsymbol{u}) = 0$ or equivalently $\nabla \cdot \boldsymbol{D}(\boldsymbol{u}) = 0$ is forced inside $\mathcal{P}(t)$, or (ii) through the explicit treatment of $-\frac{\rho_f}{\rho_p} \frac{d\boldsymbol{U}_i}{dt}$ and $-\frac{\rho_f}{\rho_p} \frac{d\boldsymbol{J}_i \boldsymbol{\omega}_i}{dt}$ [72, 82]. The variational formulation Eq (5.12)-Eq (5.15) naturally leads to a Finite Element spatial discretization [25, 26, 27, 28], but this set of equations can be re-written in a non-variational form such that other spatial discretization schemes can be used such as Finite Difference [110, 111, 115, 113, 114] and Finite Volume [72, 104, 17, 82].

Eq (5.12)-Eq (5.15) is a saddle-point problem corresponding to a constrained minimization problem. The first constraint is the usual fluid velocity divergence free, relaxed with the pressure p as a Lagrange multiplier, while the second constraint is the rigid body motion inside particles, relaxed

with the distributed Lagrange multiplier λ . This problem is solved by an Uzawa algorithm. The expression of the hydrodynamic force and torque exerted on each particle can be derived from Eq (5.13) by simple identification with a classical way of writing Newton's law for each particle, and reads as follows:

$$\mathbf{F}_{h,i} = \int_{\mathcal{P}_i(t)} \lambda d\mathbf{x} + \frac{\rho_f}{\rho_p} M_i \frac{d\mathbf{U}_i}{dt}, \quad (5.16)$$

$$\mathbf{T}_{h,i} = \int_{\mathcal{P}_i(t)} \mathbf{r} \times \lambda d\mathbf{x} + \frac{\rho_f}{\rho_p} M_i \frac{d\mathbf{J}_i \boldsymbol{\omega}_i}{dt} \quad (5.17)$$

If we re-write $\sum_{i=0}^{N-1} \int_{\mathcal{P}_i(t)} \lambda \cdot \mathbf{v} d\mathbf{x} = \mathbf{f}$ in Eq (5.12), the resulting equation is similar to an IB method with the two fundamental differences:

1. the forcing term \mathbf{f} is implicit in the original DLM/FD formulation while it is explicit in the vast majority of IB formulations.
2. the forcing term \mathbf{f} is active in the particle volume and on the particle surface in DLM/FD methods while it is active on the particle surface only in the vast majority of IB formulations.

The implicit computation of the distributed Lagrange multiplier λ and consequently of the hydrodynamic force and torque equips the original DLM/FD formulation with strong stability properties, in particular as a function of the density ratio ρ_f/ρ_p . However, there is a corresponding additional computing overhead associated to the iterative process of the Uzawa algorithm or its preconditioned conjugate gradient variant. Note that in practice, Eq (5.12)-Eq (5.15) are never solved in a monolithic fashion (with the exception of [108]) but instead with a fractional step time algorithm [25, 111, 104]. To avoid the computing overhead related to the Uzawa algorithm, many authors have derived DLM/FD formulations with an explicit equation for the distributed Lagrange multiplier λ [84, 101, 112, 23]. These direct-forcing DLM/FD formulations are indeed very close to the direct-forcing IB formulations discussed in § 5.2. The many variants of DLM/FD or closely related methods differ in the way the distributed Lagrange multiplier λ or the corresponding forcing term \mathbf{f} is discretized on the grid (Lagrangian versus Eulerian representation, see [34, 103] for an extended discussion). An important feature, beyond the accuracy of the spatial discretization that is at best second order, is whether this discretization is gradient discontinuity capturing at the particle surface or not. The use of Finite Element basis functions or IB-type regularized Dirac kernels to transfer quantities from the Eulerian grid to the Lagrangian grid and vice-versa implicitly involve a certain degree of smearing or smoothing across the fluid-particle interface. Sharp representation of the fluid-particle interface are generally obtained with ghost node or cut-cell discretization schemes. In the context of DLM/FD methods, the implementation in [104] is gradient discontinuity capturing and can be viewed as an implicit ghost node method with additional volume forcing.

DLM/FD methods have been successfully applied to a large range of particle-laden flow problems: low to high solid volume fraction, viscous and inertial flow regimes, with spherical and non-spherical particles, and with and without heat transfer. DLM/FD implementations that represent particles on the Eulerian fluid grid by a set of points need to homogeneously distribute these points on the particle surface and in the particle volume. The particle surface distribution algorithms are similar to those utilized in IB methods discussed in § 5.2.2, adding to the long list of similarities between DLM/FD and IB [95, 104]. As expected, the spatial accuracy of the DLM/FD method is found to be on par with that of IB methods and approximately the same number of points per particle diameter is required to yield a given level of accuracy [95, 111, 112, 104]. The reader further interested in DLM/FD methods is referred to the following recent review papers [34, 103].

5.4 Boltzmann-equation based mesoscopic methods

As alternative computational fluid dynamics (CFD) methods, kinetics methods based on the Boltzmann equation have been developed over the last 30 years. Here we focus mainly on the kinetic methods that can solve the hydrodynamic equations (the Navier-Stokes and Fourier energy equations) for continuum fluids (*i.e.*, the low Knudsen number limit). The available kinetic methods of this type include the lattice Boltzmann method (LBM) [12], the lattice Boltzmann flux solver (LBFS) [85], the gas kinetic scheme (GKS) [107], the discrete unified gas kinetic scheme (DUGKS) [32, 31]. In this section, we briefly but rigorously introduce LBM and DUGKS, with LBM being an on-grid finite-difference implementation, and DUGKS being an off-grid finite-volume formulation. Their advantages and drawbacks will be briefly compared and discussed in the end.

5.4.1 From Boltzmann equation to Navier-Stokes-Fourier

Fluids consist of atoms, often arranged in molecules. In a classical molecular dynamics description of a gas or liquid we follow individual molecules by solving their Newtonian equations of motion that include interaction forces between the molecules [2, 22]. In a continuum approach the discrete (molecular) nature of matter is abandoned to make place for a description in terms of functions describing properties (pressure, density, velocity, temperature) that continuously depend on location in space and on time. Kinetic theory is a description in between the molecular (*microscopic*) and the continuum (*macroscopic*) description, and is usually called *mesoscopic*.

The starting point of the mesoscopic description is Boltzmann's concept of the distribution function $f(\mathbf{x}, \boldsymbol{\xi}, t)$ with \mathbf{x} location, $\boldsymbol{\xi}$ velocity, and t time. It represents the density of molecules in physical space as well as in velocity space. The SI unit of the distribution function is $[f] = \text{kg} \cdot \frac{1}{\text{m}^3} \cdot \frac{1}{(\text{m/s})^3}$.

The total time derivative of the distribution function is

$$\frac{df}{dt} = \frac{\partial f}{\partial t} + \frac{\partial f}{\partial x_\beta} \frac{dx_\beta}{dt} + \frac{\partial f}{\partial \xi_\beta} \frac{d\xi_\beta}{dt}, \quad (5.18)$$

where we use index notation for the location (x_β) and velocity (ξ_β) vector components and the summation convention (we sum over repeated Greek indices). In (5.18), $\frac{dx_\beta}{dt} = \xi_\beta$ and $\frac{d\xi_\beta}{dt}$ is acceleration per unit volume and therefore $\frac{d\xi_\beta}{dt} = \frac{F_\beta}{\rho}$ with ρ density and \mathbf{F} (external) force per unit volume. Collisions between molecules are reasons for change of the distribution function since they re-distribute momentum over the velocity space. Combining the above notions leads to the Boltzmann equation

$$\frac{\partial f}{\partial t} + \xi_\beta \frac{\partial f}{\partial x_\beta} + \frac{F_\beta}{\rho} \frac{\partial f}{\partial \xi_\beta} = \Omega(f), \quad (5.19)$$

where $\Omega(f)$ is the collision operator. It depends on the distribution function, *i.e.* on the way mass is locally distributed over velocity space. The Boltzmann equations is an advection equation with forces and collisions as source terms. In a molecular collision, mass, momentum and kinetic energy are conserved so that three basic properties of the collision operator are

$$\iiint \Omega(f) d^3\xi = 0, \quad (5.20)$$

$$\iiint \boldsymbol{\xi} \Omega(f) d^3\xi = \mathbf{0}, \quad (5.21)$$

$$\iiint \frac{\xi^2}{2} \Omega(f) d^3\xi = 0. \quad (5.22)$$

A lot of physics goes into the collision operator as it – in principle – involves a wide spectrum of collision scenarios and intermolecular forces. In this context it is worthwhile highlighting the equilibrium distribution. If a volume of gas is left by itself for long enough time, kinetic theory states that as a result of collisions its distribution function evolves towards an equilibrium distribution, the Maxwell-Boltzmann distribution:

$$f^{eq}(\mathbf{x}, \boldsymbol{\xi}, t) = \rho \left(\frac{1}{2\pi RT} \right)^{3/2} e^{-|\mathbf{c}|^2/(2RT)} \quad (5.23)$$

where $\mathbf{c} \equiv \boldsymbol{\xi} - \mathbf{u}$ is the peculiar velocity, \mathbf{u} is the mean molecular or local hydrodynamic velocity, T is temperature and m is molar mass, and R is the universal gas constant.

In the limit of a very small Knudsen number (*i.e.*, the ratio of molecular mean free path to system length scale), the macroscopic equations governing the fluid continuum can be derived from the Boltzmann equation (5.19). A mass balance equation follows from integrating the Boltzmann equation over the velocity space; a momentum balance equation follows from multiplying the Boltzmann equation with velocity and then integrating over velocity space; and an energy balance equation is obtained by multiplying the Boltzmann equation with $\xi^2/2$ and then integrating over velocity space. An interesting insight from these derivations is the realization that viscous stress $\tau_{\alpha\beta}$ and heat flux q_α are the results of deviations of distribution functions from equilibrium, namely,

$$\tau_{\alpha\beta} = - \iiint (\xi_\alpha - u_\alpha)(\xi_\beta - u_\beta) (f - f^{eq}) d^3\xi, \quad (5.24)$$

$$q_\alpha = \iiint \frac{|\boldsymbol{\xi} - \mathbf{u}|^2}{2} (\xi_\alpha - u_\alpha) f d^3\xi. \quad (5.25)$$

When the Boltzmann equation is used as a numerical algorithm for continuum fluids, a simplified collision operator, known as the Bhatnagar, Gross & Krook (BGK) collision operator [7], is often assumed

$$\Omega(f) = -\frac{1}{\tau} (f - f^{eq}), \quad (5.26)$$

namely, the collision process relaxes the distribution towards the equilibrium with a single relaxation time τ .

When τ is assumed a small parameter, equivalent to the assumption of very low Knudsen number, one can approximate f as

$$f = f^{eq} - \tau \left[\frac{\partial f^{eq}}{\partial t} + \xi_\beta \frac{\partial f^{eq}}{\partial x_\beta} + \frac{F_\beta}{\rho} \frac{\partial f^{eq}}{\partial \xi_\beta} \right] + \mathcal{O}(\tau^2), \quad \text{with} \quad \frac{\partial f^{eq}}{\partial \xi_\beta} = -\frac{(\xi_\beta - u_\beta)}{RT} f^{eq} + \mathcal{O}(\tau), \quad (5.27)$$

which is known as the Chapman-Enskog approximation. It is through this approximation that the external force term can be moved to the right-hand side of the Boltzmann equation and be treated similarly as the collision term. Eq. (5.19) together with Eqs. (5.26) and (5.23) defines a model Boltzmann equation,

$$\frac{\partial f}{\partial t} + \xi_\beta \frac{\partial f}{\partial x_\beta} = -\frac{(f - f^{eq})}{\tau} + \frac{F_\beta(\xi_\beta - u_\beta)}{\rho RT} f^{eq} \equiv \tilde{\Omega}. \quad (5.28)$$

Note that the collision term is modified to include the external force term, and the extended collision term is denoted by $\tilde{\Omega}$.

Eq. (5.27) provides the needed closure scheme for the viscous stress and the heat flux, up to the order $O(\tau)$. It is straightforward to show that the macroscopic continuity, momentum, and energy equations are

$$\frac{\partial \rho}{\partial t} + \frac{\partial (\rho u_\beta)}{\partial x_\beta} = 0, \quad (5.29)$$

$$\frac{\partial}{\partial t} (\rho u_\alpha) + \frac{\partial}{\partial x_\beta} (\rho u_\alpha u_\beta) = -\frac{\partial p}{\partial x_\alpha} + \frac{\partial \sigma_{\alpha\beta}}{\partial x_\beta} + F_\alpha, \quad (5.30)$$

$$\text{with } \sigma_{\alpha\beta} = \mu \left(\frac{\partial u_\alpha}{\partial x_\beta} + \frac{\partial u_\beta}{\partial x_\alpha} - \frac{2}{3} \delta_{\alpha\beta} \frac{\partial u_\gamma}{\partial x_\gamma} \right) + \mu^V \delta_{\alpha\beta} \frac{\partial u_\gamma}{\partial x_\gamma}, \quad (5.31)$$

$$\frac{\partial}{\partial t} (\rho e) + \frac{\partial}{\partial x_\beta} (\rho u_\beta e) = -p \frac{\partial u_\beta}{\partial x_\beta} - \frac{\partial}{\partial x_\beta} (q_\beta) + \sigma_{\alpha\beta} \frac{\partial u_\alpha}{\partial x_\beta}, \quad (5.32)$$

$$\text{with } q_\beta = -k \frac{\partial T}{\partial x_\beta}. \quad (5.33)$$

where the pressure is related to the temperature by the ideal gas equation of state $p = \rho RT$, the internal energy $e = C_v T$ with the specific heat at constant volume $C_v = 3R/2$, the specific heat at constant pressure $C_p = 5R/2$, the dynamic shear viscosity $\mu = p\tau$, and the conductivity $k = C_p p\tau$. The value of bulk viscosity μ^V depends on whether T is treated as a variable (the general compressible fluid) or is assumed to be a constant (*i.e.*, so-called athermal model): for the former case $\mu^V = 0$, and the latter case $\mu^V = 2\mu/3$. The simple model above yields a specific heat ratio of 5/3 and a Prandtl number of unity. The value of specific heat ratio can be adjusted by introducing additional internal degrees of freedom [31], and the value of Prandtl number can be adjusted in several ways, *e.g.*, by altering the equilibrium distribution or by adding a properly designed source term [13].

What we have set up is an algorithm that uses a simplified Boltzmann equation to represent the Navier-Stokes-Fourier system, Eqs. (5.29) through (5.33). The essential idea of the mesoscopic methods is to numerically solve Eq. (5.28) instead of the Navier-Stokes-Fourier system directly. Two methods of solving Eq. (5.28) are presented next.

5.4.2 The on-grid lattice-Boltzmann method

The lattice-Boltzmann equation (LBE) is an efficient method to solve the model Boltzmann equation such as Eq. (5.28). It involves a triple discretization of the model Boltzmann equation: space \mathbf{x} , time t , and particle velocity $\boldsymbol{\xi}$. The discrete velocity set of size $n + 1$ is denoted as $\mathbf{e}_i, i = 0 \dots n$, the distribution function as $f_i(\mathbf{x}, t)$ which is now understood as the density of molecules at location \mathbf{x} and time t having velocity \mathbf{e}_i . Integrating Eq. (5.28) along the path associated with \mathbf{e}_i , from t to $t + dt$, using the trapezoidal rule for the right hand side, one obtains

$$f_i(\mathbf{x} + \mathbf{e}_i dt, t + dt) - f_i(\mathbf{x}, t) = \frac{dt}{2} \left[\tilde{\Omega}_i(\mathbf{x}, t) + \tilde{\Omega}_i(\mathbf{x} + \mathbf{e}_i dt, t + dt) \right]. \quad (5.34)$$

To remove the time implicity, a linear transformation is introduced

$$\tilde{f}_i(\mathbf{x}, t) = f_i(\mathbf{x}, t) - \frac{dt}{2} \tilde{\Omega}_i(\mathbf{x}, t), \quad (5.35)$$

It is straightforward to show that Eq. (5.34) can then be written in an explicit form as

$$\tilde{f}_i(\mathbf{x} + \mathbf{e}_i dt, t + dt) = \tilde{f}_i(\mathbf{x}, t) - \frac{(\tilde{f}_i - f_i^{eq})}{\tau_L} + \left[1 - \frac{1}{2\tau_L} \right] \frac{F_\beta(e_{i,\beta} - u_\beta)}{\rho RT} f_i^{eq} dt, \quad (5.36)$$

where

$$\tau_L = \frac{\tau}{dt} + \frac{1}{2} = \frac{\nu}{c_s^2 dt} + \frac{1}{2}, \quad \text{or } \nu = \left(\tau_L - \frac{1}{2} \right) c_s^2 dt, \quad (5.37)$$

where ν is the fluid kinematic viscosity.

An important step in deriving LBE is to convert the integral velocity moments into discrete summations over \mathbf{e}_i , a process known as the Gauss-Hermite quadratures. This amounts to a multiplication of a pre-factor involving only \mathbf{e}_i , namely, $g_i = w_i (2\pi RT)^{D/2} \exp[e_i^2 / (2RT)] \tilde{f}$. The linearity of Eq. (5.36) implies that g_i is governed by

$$g_i(\mathbf{x} + \mathbf{e}_i dt, t + dt) = g_i(\mathbf{x}, t) - \frac{(g_i(\mathbf{x}, t) - g_i^{eq}(\mathbf{x}, t))}{\tau_L} + \left[1 - \frac{1}{2\tau_L} \right] \frac{F_\beta(e_{i,\beta} - u_\beta)}{\rho RT} g_i^{eq}(\mathbf{x}, t) dt, \quad (5.38)$$

where, for isothermal flows, the Hermite expansion [83] of the equilibrium yield

$$g_i^{eq} = w_i \rho \left[1 + \frac{u_\alpha e_{i\alpha}}{c_s^2} + \frac{(u_\alpha e_{i\alpha})^2}{2c_s^4} - \frac{u^2}{2c_s^2} + \frac{(u_\alpha e_{i\alpha})^3}{6c_s^6} - \frac{(u_\alpha e_{i\alpha})u^2}{2c_s^4} \right], \quad (5.39)$$

where $c_s^2 = RT$, w_i a set of weighing factors that depend on the exact definition of the velocity set \mathbf{e}_i (or from the Gauss-Hermite quadrature requirements), and $c_s = \sqrt{RT}$. The terms of $O(u^3)$ is included here to ensure that the Navier-Stokes equation is exactly recovered under the Chapman-Enskog approximation [83]. Eq. (5.38) is the well-known LBE, here derived from the model Boltzmann equation with the external force term included as a source term.

Under the Gauss-Hermite quadratures, the hydrodynamic moments for isothermal flow can be written as

$$\rho(\mathbf{x}, t) = \sum_{i=0}^n g_i(\mathbf{x}, t), \quad (5.40)$$

$$\rho(\mathbf{x}, t) \mathbf{u}(\mathbf{x}, t) = \sum_{i=0}^n \mathbf{e}_i g_i(\mathbf{x}, t) + \frac{\mathbf{F} dt}{2}. \quad (5.41)$$

For computational efficiency, it is desirable to choose a lattice velocity model with a small n .

The lattice Boltzmann method is an *on-grid* implementation method, meaning that the modeled “molecules” travel from a lattice node to a neighbouring node, or stay where they were if $\mathbf{e}_i = \mathbf{0}$. While this on-grid implementation makes the coding very simple and advection formally precise, it has two obvious disadvantages. First, the space lattice grid has to be geometrically simple (*e.g.*, hexagon and square cells in 2D). Second, the on-grid implementation limits the choices of the velocity set \mathbf{e}_i or alternatively the achievable quadrature order of velocity moments of g_i ; the latter is essential for the proper recovery of the hydrodynamic equations. For a square or cubic grid, $dx = e_{i1} dt$ and the fifth-order Gauss-Hermite quadrature would require $e_{i1} = \sqrt{3RT}$. For convenience, dx is taken as the space unit and dt the time unit in the lattice Boltzmann method, leading to setting $c_s^2 = RT = 1/3$ in the standard LB scheme.

A time step in an LB algorithm consists of executing (5.38) for every node of the lattice. For this we need the equilibrium distribution function in each node (5.39) and therefore density and velocity in each node. For the latter two variables we use (5.40) and (5.41). For isothermal flow, it follows that

$$p = \rho c_s^2. \quad (5.42)$$

Since equation (5.42) implies that $\partial p / \partial \rho = c_s^2$, c_s can be interpreted as the speed of sound which is finite in an LB scheme. This can be easily understood since a distribution function – and therefore

information – only travels to a neighbouring node over one time step. An LB scheme therefore is a compressible scheme for which a Mach number can be defined:

$$M \equiv |\mathbf{u}|/c_s. \quad (5.43)$$

An often used velocity set in two dimensions is named D2Q9 (two dimensions, nine velocities); an often used set in three dimensions is D3Q19. For reference we give here their definitions, i.e. the discrete set of velocities in Cartesian coordinates and weighting factors.

D2Q9:

$$\begin{aligned} \mathbf{e}_0 &= \begin{pmatrix} 0 \\ 0 \end{pmatrix}, \mathbf{e}_1 = \begin{pmatrix} 1 \\ 0 \end{pmatrix}, \mathbf{e}_2 = \begin{pmatrix} -1 \\ 0 \end{pmatrix}, \mathbf{e}_3 = \begin{pmatrix} 0 \\ 1 \end{pmatrix}, \mathbf{e}_4 = \begin{pmatrix} 0 \\ -1 \end{pmatrix}, \mathbf{e}_5 = \begin{pmatrix} 1 \\ 1 \end{pmatrix}, \\ \mathbf{e}_6 &= \begin{pmatrix} -1 \\ 1 \end{pmatrix}, \mathbf{e}_7 = \begin{pmatrix} -1 \\ -1 \end{pmatrix}, \mathbf{e}_8 = \begin{pmatrix} 1 \\ -1 \end{pmatrix}, \end{aligned} \quad (5.44)$$

$$w_0 = 4/9, w_{1-4} = 1/9, w_{5-8} = 1/36. \quad (5.45)$$

D3Q19:

$$\begin{aligned} \mathbf{e}_0 &= \begin{pmatrix} 0 \\ 0 \\ 0 \end{pmatrix}, \mathbf{e}_1 = \begin{pmatrix} 1 \\ 0 \\ 0 \end{pmatrix}, \mathbf{e}_2 = \begin{pmatrix} 0 \\ 1 \\ 0 \end{pmatrix}, \mathbf{e}_3 = \begin{pmatrix} -1 \\ 0 \\ 0 \end{pmatrix}, \mathbf{e}_4 = \begin{pmatrix} 0 \\ -1 \\ 0 \end{pmatrix}, \mathbf{e}_5 = \begin{pmatrix} 0 \\ 0 \\ 1 \end{pmatrix}, \\ \mathbf{e}_6 &= \begin{pmatrix} 0 \\ 0 \\ -1 \end{pmatrix}, \mathbf{e}_7 = \begin{pmatrix} 1 \\ 1 \\ 0 \end{pmatrix}, \mathbf{e}_8 = \begin{pmatrix} -1 \\ 1 \\ 0 \end{pmatrix}, \mathbf{e}_9 = \begin{pmatrix} -1 \\ -1 \\ 0 \end{pmatrix}, \mathbf{e}_{10} = \begin{pmatrix} 1 \\ -1 \\ 0 \end{pmatrix}, \mathbf{e}_{11} = \begin{pmatrix} 1 \\ 0 \\ 1 \end{pmatrix}, \\ \mathbf{e}_{12} &= \begin{pmatrix} -1 \\ 0 \\ 1 \end{pmatrix}, \mathbf{e}_{13} = \begin{pmatrix} -1 \\ 0 \\ -1 \end{pmatrix}, \mathbf{e}_{14} = \begin{pmatrix} 1 \\ 0 \\ -1 \end{pmatrix}, \mathbf{e}_{15} = \begin{pmatrix} 0 \\ 1 \\ 1 \end{pmatrix}, \mathbf{e}_{16} = \begin{pmatrix} 0 \\ -1 \\ 1 \end{pmatrix}, \\ \mathbf{e}_{17} &= \begin{pmatrix} 0 \\ -1 \\ -1 \end{pmatrix}, \mathbf{e}_{18} = \begin{pmatrix} 0 \\ 1 \\ -1 \end{pmatrix}, \end{aligned} \quad (5.46)$$

$$w_0 = 1/3, w_{1-6} = 1/18, w_{7-18} = 1/36. \quad (5.47)$$

The *on-grid* implementation in the LB algorithm makes it difficult to design a lattice velocity model which has a sufficient order to recover the hydrodynamic equations. Even for an isothermal flow, an important observation of the Chapman-Enskog approximation is that the viscous stress would require the third-order moment of the equilibrium distribution be computed correctly; this requires the lattice velocity model to have at least a sixth-order Gauss-Hermite quadrature accuracy. Unfortunately, both D2Q9 and D3Q19 only have a fifth order quadrature accuracy, then there is an error (proportional to M^3) in computing the viscous-stress moment. For this reason, the standard LB algorithm makes the assumption of low-Mach number or incompressible flow, thus we need to make sure that $M \ll 1$ everywhere in the domain. With c_s of order one (in lattice units $\Delta/\Delta t$), the $M \ll 1$ condition then implies $|\mathbf{u}| = |\mathbf{u}|\Delta t/\Delta \ll 1$. The latter expression shows that absolute velocity in lattice units is equivalent to a Courant number. The LB scheme is explicit, see (5.38). The incompressibility constraint is therefore a much stronger constraint than the CFL stability condition $|\mathbf{u}|\Delta t/\Delta < 1$ [21] that usually applies to explicit schemes. In practical terms one designs simulations such that the Mach number stays below 0.1 [12].

5.4.3 The generalized off-grid DUGKS method

In DUGKS, we instead apply a finite-volume treatment to Eq. (5.28). In this approach, the discrete particle velocities \mathbf{e}_i are no longer coupled with the space lattice. This comes with two advantages: first, the choice of the discrete velocity set $\{\mathbf{e}_i\}$ can be better optimized to achieve the required Gauss-Hermite order of accuracy; second, a non-uniform or unstructured mesh can be easily incorporated. It should also be noted that the model Boltzmann equation, Eq. (5.28), is a more general description of fluid motion which can be used to treat flows at arbitrary Knudsen numbers. For these reasons, DUGKS have been used to simulate a variety of flows including thermal compressible or non-continuum flows.

To this end, the distribution function is first generalized to include additional degrees of freedom, written as $f(\mathbf{x}, \boldsymbol{\xi}, \boldsymbol{\eta}, \zeta, t)$, where $\mathbf{x} = (x_1, \dots, x_D)$ and $\boldsymbol{\xi} = (\xi_1, \dots, \xi_D)$, D is the spatial dimension of the hydrodynamic velocity u_i , $\boldsymbol{\eta}$ denotes the remaining $(3 - D)$ space of the microscopic velocity, an internal kinetic variable, ζ , of dimension K is introduced in order to adjust the specific heat ratio of the model. Second, a source term S_f is included to allow for arbitrary Prandtl number and different ratios of bulk to shear viscosity, as well as a source term in the macroscopic energy equation. Then Eq. (5.28) and Eq. (5.23) become

$$\frac{\partial f}{\partial t} + \xi_\beta \frac{\partial f}{\partial x_\beta} = -\frac{(f - f^{eq})}{\tau} + \frac{F_\beta(\xi_\beta - u_\beta)}{\rho RT} f^{eq} + S_f. \quad (5.48)$$

$$f^{eq} = \frac{\rho}{(2\pi RT)^{(3+K)/2}} \exp\left(-\frac{c^2 + \eta^2 + \zeta^2}{2RT}\right), \quad (5.49)$$

The internal energy e per unit mass and the heat flux are now formulated by

$$\rho e = \int \frac{(c^2 + \eta^2 + \zeta^2)}{2} f d\xi d\boldsymbol{\eta} d\zeta, \quad q_\beta = \frac{1}{2} \int c_\beta (c^2 + \eta^2 + \zeta^2) f d\xi d\boldsymbol{\eta} d\zeta. \quad (5.50)$$

For efficient numerical implementation, we first integrate over $(\boldsymbol{\eta}, \zeta)$, and introduce two reduced distributions $g(\mathbf{x}, \boldsymbol{\xi}, t)$ and $h(\mathbf{x}, \boldsymbol{\xi}, t)$ [31]:

$$g(\mathbf{x}, \boldsymbol{\xi}, t) = \int f(\mathbf{x}, \boldsymbol{\xi}, \boldsymbol{\eta}, \zeta, t) d\boldsymbol{\eta} d\zeta, \quad h(\mathbf{x}, \boldsymbol{\xi}, t) = \int (\eta^2 + \zeta^2) f(\mathbf{x}, \boldsymbol{\xi}, \boldsymbol{\eta}, \zeta, t) d\boldsymbol{\eta} d\zeta. \quad (5.51)$$

Correspondingly, the governing equations for $g(\mathbf{x}, \boldsymbol{\xi}, t)$ and $h(\mathbf{x}, \boldsymbol{\xi}, t)$ can be obtained from Eq. (5.48) as:

$$\frac{\partial g}{\partial t} + \boldsymbol{\xi} \cdot \nabla_{\mathbf{x}} g = -\frac{g - g^{eq}}{\tau} + \frac{F_\beta(\xi_\beta - u_\beta)}{\rho RT} g^{eq} + S_g, \quad (5.52a)$$

$$\frac{\partial h}{\partial t} + \boldsymbol{\xi} \cdot \nabla_{\mathbf{x}} h = -\frac{h - h^{eq}}{\tau} + \frac{F_\beta(\xi_\beta - u_\beta)}{\rho RT} h^{eq} + S_h, \quad (5.52b)$$

where $S_g = \int S_f d\boldsymbol{\eta} d\zeta$, $S_h = \int (\eta^2 + \zeta^2) S_f d\boldsymbol{\eta} d\zeta$, the reduced equilibriums g^{eq} and h^{eq} are

$$g^{eq} = \int f^{eq} d\boldsymbol{\eta} d\zeta = \frac{\rho}{(2\pi RT)^{D/2}} \exp\left[-\frac{(\boldsymbol{\xi} - \mathbf{u})^2}{2RT}\right], \quad (5.53a)$$

$$h^{eq} = \int (\eta^2 + \zeta^2) f^{eq} d\boldsymbol{\eta} d\zeta = (K + 3 - D) RT g^{eq}. \quad (5.53b)$$

Using the Chapman-Enskog approximation, it can be shown that the above system will reproduce the fully compressible Navier-Stokes-Fourier system, Eqs. (5.29) - (5.33), with a shear viscosity $\mu = p\tau$. The expressions for the bulk viscosity μ^V and conductivity k depend on the details of the source term S_f , as shown in [106, 13].

Next, we describe the DUGKS algorithm. Eqs. (5.52a) and (5.52b) which can be written as

$$\frac{\partial \phi}{\partial t} + \boldsymbol{\xi} \cdot \nabla_x \phi = \tilde{\Omega}_\phi = \Omega_\phi + Q_\phi, \quad (5.54)$$

where $\phi = g$ or h , $Q_\phi = \phi^{eq} [F_\beta(\xi_\beta - u_\beta)] / (\rho RT)$.

As a finite-volume method, the first step is to decompose the computational domain into a set of control volumes. Eq. (5.54) is integrated over a cell V_j located at \mathbf{x}_j from time t_n to t_{n+1} . The time integration is done using the mid-point rule for the convection term and the trapezoidal rule for the collision term, then the evolution equation becomes

$$\tilde{\phi}_j^{n+1} = \tilde{\phi}_j^{+,n} - \frac{\Delta t}{|V_j|} F^{n+\frac{1}{2}}, \quad F^{n+\frac{1}{2}} \equiv \int_{\partial V_j} (\boldsymbol{\xi} \cdot \mathbf{n}) \phi(\boldsymbol{\xi}, \mathbf{x}, t_{n+1/2}) dS, \quad (5.55)$$

where the time implicity has been removed by introducing the following linear transformations

$$\tilde{\phi} = \phi - \frac{\Delta t}{2} \tilde{\Omega}_\phi, \quad \tilde{\phi}^+ = \phi + \frac{\Delta t}{2} \tilde{\Omega}_\phi, \quad (5.56)$$

and they are understood as cell-averaged values, $F^{n+\frac{1}{2}}$ is the microscopic flux across the cell interface at $t_{n+1/2} \equiv t_n + 0.5\Delta t$, and \mathbf{n} is the outward unit vector normal to the cell interface located at \mathbf{x}_b .

All hydrodynamic variables can be obtained from the auxiliary distribution $\tilde{\phi}$ directly. For the evolution of Eq. (5.55), the key step is to evaluate the microscopic flux $F^{n+\frac{1}{2}}$ at the cell interface at half time step which requires the reconstruction of the original distribution $\phi(\boldsymbol{\xi}, \mathbf{x}_b, t_{n+1/2})$. In order to obtain that, we integrate the Boltzmann equation Eq. (5.54) for a half time step $s = \frac{\Delta t}{2}$, from t_n to $t_n + 0.5\Delta t$, along the characteristic line with the end point located at the cell interface \mathbf{x}_b , again the trapezoidal rule is applied to the collision term:

$$\phi(\boldsymbol{\xi}, \mathbf{x}_b, t_{n+1/2}) - \phi(\boldsymbol{\xi}, \mathbf{x}_b - \boldsymbol{\xi}s, t_n) = \frac{s}{2} [\tilde{\Omega}_\phi(\boldsymbol{\xi}, \mathbf{x}_b, t_{n+1/2}) + \tilde{\Omega}_\phi(\boldsymbol{\xi}, \mathbf{x}_b - \boldsymbol{\xi}s, t_n)]. \quad (5.57)$$

Once again to remove time implicity, another two auxiliary distributions $\bar{\phi} = \phi - (s/2)\tilde{\Omega}_\phi$ and $\bar{\phi}^+ = \phi + (s/2)\tilde{\Omega}_\phi$ are introduced. And Taylor expansion around the node $(\boldsymbol{\xi}, \mathbf{x}_b, t_n)$ is applied to $\bar{\phi}^+(\boldsymbol{\xi}, \mathbf{x}_b - \boldsymbol{\xi}s, t_n)$:

$$\bar{\phi}(\boldsymbol{\xi}, \mathbf{x}_b, t_{n+1/2}) = \bar{\phi}^+(\boldsymbol{\xi}, \mathbf{x}_b - \boldsymbol{\xi}s, t_n) = \bar{\phi}^+(\boldsymbol{\xi}, \mathbf{x}_b, t_n) - \boldsymbol{\xi}s \cdot \boldsymbol{\sigma}_b, \quad (5.58)$$

where $\boldsymbol{\sigma}_b = \nabla_x \bar{\phi}^+(\boldsymbol{\xi}, \mathbf{x}_b, t_n)$. It is obvious that the right-hand side of the Eq. (5.58) is explicit, $\bar{\phi}^+$ can be obtained by interpolation and the slope $\boldsymbol{\sigma}_b$ can be estimated from the difference between the two neighboring cells for smooth flows. Hydrodynamic variables at time $t_{n+1/2}$ can be computed from the distribution function $\bar{\phi}(\boldsymbol{\xi}, \mathbf{x}_b, t_{n+1/2})$. Then the equilibrium ϕ^{eq} can be obtained and the original distribution can be computed from $\bar{\phi}$:

$$\phi(\boldsymbol{\xi}, \mathbf{x}_b, t_{n+1/2}) = \frac{2\tau}{2\tau + s} \bar{\phi}(\boldsymbol{\xi}, \mathbf{x}_b, t_{n+1/2}) + \frac{s}{2\tau + s} \phi^{eq}(\boldsymbol{\xi}, \mathbf{x}_b, t_{n+1/2}) + \frac{\tau s}{2\tau + s} Q_\phi. \quad (5.59)$$

With the original distribution $\phi(\boldsymbol{\xi}, \mathbf{x}_b, t_{n+1/2})$ computed at the cell interface \mathbf{x}_b at time $t_{n+1/2}$, the microscopic flux $F^{n+\frac{1}{2}}$ can be obtained. The distributions at t_{n+1} can then be obtained from Eq. (5.55).

In the numerical implementation, the equilibrium distribution should be expanded to fourth order for thermal flows, or third order for the isothermal flows [105]. The required order for Gauss quadrature is thus eighth order for thermal flow and sixth order for isothermal flows, although this can be relaxed when the flow Mach number is small.

In terms of the distributions for the discrete velocities, the hydrodynamic variables can be evaluated as

$$\rho = \sum_{\alpha} \tilde{g}_{\alpha} = \sum_{\alpha} \tilde{g}_{\alpha}^{+} = \sum_{\alpha} \bar{g}_{\alpha} = \sum_{\alpha} \bar{g}_{\alpha}^{+}, \quad (5.60a)$$

$$\rho \mathbf{u} = \sum_{\alpha} \xi_{\alpha} \tilde{g}_{\alpha} + \frac{dt}{2} \mathbf{b} = \sum_{\alpha} \xi_{\alpha} \tilde{g}_{\alpha}^{+} - \frac{dt}{2} \mathbf{b} = \sum_{\alpha} \xi_{\alpha} \bar{g}_{\alpha} + \frac{s}{2} \mathbf{b} = \sum_{\alpha} \xi_{\alpha} \bar{g}_{\alpha}^{+} - \frac{s}{2} \mathbf{b}, \quad (5.60b)$$

$$\rho \left(C_V T + \frac{u^2}{2} \right) = \frac{1}{2} \sum_{\alpha} (\xi_{\alpha}^2 \tilde{g}_{\alpha} + \tilde{h}_{\alpha}) + \frac{\Delta t}{2} \rho \mathbf{u} \cdot \mathbf{b} = \frac{1}{2} \sum_{\alpha} (\xi_{\alpha}^2 \bar{g}_{\alpha} + \bar{h}_{\alpha}) + \frac{s}{2} \rho \mathbf{u} \cdot \mathbf{b}. \quad (5.60c)$$

Therefore, $\rho(\mathbf{x}_b, t_n + s)$ and $\mathbf{u}(\mathbf{x}, t_n + s)$ can be obtained from $\bar{g}_{\alpha}(\mathbf{x}_b, t_n + s)$, which can be used to compute $f_{\alpha}^{(eq)}(\mathbf{x}_b, t_n + s)$.

When compared to the treatment of the nonlinear advection term in the conventional Navier-Stokes solvers, we observe two important differences: (1) the advection or related flux term in DUGKS is linear and as such the time evolution from t_n for $t_n + s$, Eq. (5.57), is formally precise, (2) the interpolation here is over space only at a single time t_n while the interpolation in the Navier-Stokes solvers involves both space and time. The coupled collision and streaming treatment in Eq. (5.57) is exact, and the space-only interpolation in Eq. (5.58) maintains a low numerical dissipation of the overall scheme. A mathematical analysis of the numerical dissipation in DUGKS [123] shows that the former depends on both the mesh size and the time step size (or equivalently the CFL number), but is smaller than a version which uses a direct interpolation without considering the collision term.

5.4.4 Treating the moving solid-fluid interfaces

Both LBM and DUGKS have been applied to simulate suspension flows, turbulent flows, and turbulent flows laden with finite-size particles. The theoretical and practical groundwork for particle-resolved suspension simulations through an LB approach was laid in two papers by Ladd [50, 51]. The papers are not only among the first in terms of approximately resolved suspension simulations, they also give a comprehensive account of the LB method and the way it relates to Newtonian fluid dynamics and how moving no-slip boundaries can be accounted for. In Ladd's approach, the location of the no-slip surface is halfway the link between two lattice nodes that is cut by the surface, due to the simple (or half-way) bounce back implemented as

$$f_i(\mathbf{x}_f, t + dt) = f_i^*(\mathbf{x}_f, t) + 2\rho w_i \frac{\mathbf{e}_i \cdot \mathbf{u}_w}{c_s^2}, \quad (5.61)$$

where \mathbf{x}_f denotes the location of a fluid node near the solid boundary, \mathbf{e}_i denotes a direction coming from the wall, and $\mathbf{e}_i = -\mathbf{e}_i$, f_i^* denotes the right hand side of Eq. (5.38) or the value after collision, \mathbf{u}_w is the local wall velocity. This results in a stair-step boundary condition that approaches the actual surface upon refining the lattice. There is fluid inside the particle surfaces which is kept there for convenience. This internal fluid is often considered to be decoupled from the external fluid. The convenience lies in the fact that this approach avoids the need for creating fluid when a moving particle uncovers a node and destroying fluid when it covers a node. Reference [51] deals with a number of practicalities when applying the approach to multiple spherical particles suspended in fluid.

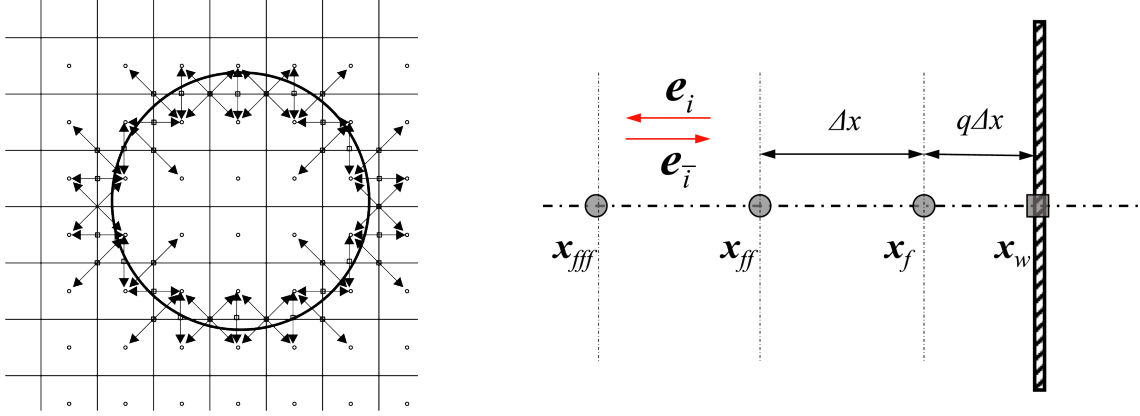


Figure 5.3: Left panel: Half-way bounce-back representation of a circular no-slip boundary on a square lattice. Circular dots are lattice nodes sitting in the centre of square cells. The bounce-back conditions representing no-slip are imposed halfway the links between those two nodes that intersect with the circle (square dots) [51]. Right panel: sketch used to illustrate the interpolated bounce-back scheme.

The stair-step boundaries and associated particle shape fluctuations when a particle moves over the lattice have motivated the interpolated bounce-back scheme or the use of immersed boundaries in LB simulations. It is well known that Eq. (5.61) is only of first-order accuracy for a curved fluid-solid surface. In order to ensure the second-order spatial accuracy in a bounce-back process, a number of interpolated bounce-back (IBB) schemes have been introduced over the years, with the conditional IBB scheme proposed by Bouzidi et al. [8] and the unified IBB scheme by Yu et al. [109] being the most representative. The location of the solid wall is defined by $q = |\mathbf{x}_f - \mathbf{x}_w|/|\mathbf{x}_f - \mathbf{x}_b|$ (see Figure 5.3 (b)). In Bouzidi et al.'s scheme, when $q < 0.5$, a virtual distribution function is interpolated first so that the particle represented by this virtual distribution function ends precisely at \mathbf{x}_f after the bounce back. On the other hand, when $q \geq 0.5$, the bounce back of distribution f_i^* is performed first, and then interpolated back to \mathbf{x}_f . Namely,

$$f_i(\mathbf{x}_f, t + dt) = q(2q + 1)f_i^*(\mathbf{x}_f, t) + (1 + 2q)(1 - 2q)f_i^*(\mathbf{x}_{ff}, t) - q(1 - 2q)f_i^*(\mathbf{x}_{fff}, t) + 2\rho w_i \frac{\mathbf{e}_i \cdot \mathbf{u}_w}{c_s^2}, \quad q < 0.5, \quad (5.62)$$

$$f_i(\mathbf{x}_f, t + dt) = \frac{1}{q(2q + 1)} \left[f_i^*(\mathbf{x}_f, t) + 2\rho w_i \frac{\mathbf{e}_i \cdot \mathbf{u}_w}{c_s^2} \right] + \frac{2q - 1}{q} f_i(\mathbf{x}_{ff}, t + dt) - \frac{2q - 1}{1 + 2q} f_i(\mathbf{x}_{fff}, t + dt), \quad q \geq 0.5, \quad (5.63)$$

Alternatively, Yu et al. designed a unified IBB scheme for all values of q . First, a virtual distribution function is interpolated between \mathbf{x}_f and \mathbf{x}_{ff} , which ends exactly at the wall location after streaming a grid spacing towards the wall. Next, an instantaneous bounce-back happens right after the virtual distribution function arrives at the wall location. Finally, the unknown distribution function is interpolated from this distribution and that at \mathbf{x}_{ff} . Together, this yields

$$f_i(\mathbf{x}_f, t + dt) = \frac{q}{(2 + q)} f_i^*(\mathbf{x}_f, t) + \frac{2(1 - q)}{(1 + q)} f_i^*(\mathbf{x}_{ff}, t) - \frac{(1 - q)q}{(1 + q)(2 + q)} f_i^*(\mathbf{x}_{fff}, t) + \frac{2q}{1 + q} f_i(\mathbf{x}_{ff}, t + dt) - \frac{q}{2 + q} f_i(\mathbf{x}_{fff}, t + dt) + \frac{4}{(1 + q)(2 + q)} \rho w_i \frac{\mathbf{e}_i \cdot \mathbf{u}_w}{c_s^2} \quad (5.64)$$

In both the simple bounce-back and interpolated bounce-back schemes, the momentum exchange between the particle and the solid wall during bounce-back is well defined, thus by summing these exchanges, one can easily compute the hydrodynamic force and torque acting on the solid particle.

Initial attempts to apply the immersed boundary method in the context of lattice-Boltzmann simulations were based on the feedback approach due to [29] and alluded to in the present § 5.2. The approach is to locally apply forces on the fluid that oppose a difference between the fluid velocity at the immersed boundary and the desired velocity of the immersed boundary. Iteration or time stepping then establishes and maintains the velocity condition. An early – 1999 – application of this method is the representation of an impeller in a mixing tank in single-phase large-eddy simulations [14]. The surface of the impeller is represented by a closely spaced set of off-lattice marker points with a typical nearest neighbour spacing of $0.5 - 0.7\Delta$. The fluid velocity at the marker points is determined through interpolation (linear or quadratic) from the lattice, as in Eq. (5.4). We then update the force on the fluid responsible for imposing the velocity boundary condition at Lagrangian points \mathbf{X}_l as

$$\mathbf{F}^{(n)}(\mathbf{X}_l) = \mathbf{F}^{(n-1)}(\mathbf{X}_l) + \alpha \left(\mathbf{U}^{(d)}(\mathbf{X}_l) - \tilde{\mathbf{U}}_f(\mathbf{X}_l) \right), \quad (5.65)$$

with $\mathbf{U}^{(d)}(\mathbf{X}_l)$ the velocity boundary condition and α a relaxation parameter. The final step is to distribute the forces at the Lagrangian points back to their Eulerian lattice nodes, similar to Eq. (5.6).

The stability and accuracy of the method hinges on the free parameter α [14]. Having a free parameter, as noted in § 5.2, is a disadvantage. On the positive side, the method largely retains the locality of the arithmetic operations inherent to the LB method. This feature of the LB method enables simple computational parallelization strategies.

As noted, initially the above method was applied for imposing the moving no-slip condition at the surface of a revolving impeller. Extending it to solid particles moving through fluid is straightforward [91]. Different from an impeller, however, the linear and angular motion of the particle and therefore the solid surface velocity is not known a priori and needs to be solved. This involves solving the equations of linear and rotational motion of each particle. This is the subject of § 5.2.5. The equations of motion include the hydrodynamic force and torque on each particle. These are directly available through integration of the force distribution that is responsible for imposing the immersed boundary (5.65) over the surface of the particle.

Alternative force-based immersed boundary methods in an LB context have been proposed by e.g. [19]. They stay close to the original ideas of Peskin [68] (see also Section 5.2) of an “elastic restoration force” that counteracts deformations of the immersed solid object as a result of fluid flow. The restoring forces act on off-grid marker points. They are distributed over neighbouring lattice nodes through a regularized delta function [19].

Due to the motion of virtual fluid inside the volume occupied by the solid particle in these force-based immersed boundary methods, care has to be taken when defining the hydrodynamic force/torque which enters the Newton-Euler equations for linear and angular particle acceleration. This is analogous to the discussion in § 5.2.5 leading to equation 5.10. Similarly as already discussed in § 5.2.5, a singularity arises in the limit of density-matched particles. Several authors have proposed alternatives in the context of LBM methods [20].

Returning back to the LB scheme, Eq. (5.38), the last term used to implement the external force is often simplified by inserting the Hermite expansion, Eq. (5.39), and keeping only terms up to $\mathcal{O}(Ma)$, namely,

$$\left(1 - \frac{1}{2\tau_L} \right) \frac{F_\beta (e_{i,\beta} - u_\beta)}{\rho RT} g_i^{eq}(\mathbf{x}, t) dt \approx \left(1 - \frac{1}{2\tau} \right) w_i \left(\frac{e_{i\alpha}}{c_s^2} + \frac{(e_{i\alpha} e_{i\beta} - c_s^2 \delta_{\alpha\beta}) u_\beta}{c_s^4} \right) F_\alpha dt, \quad (5.66)$$

which is the well-known Guo scheme [33].

The method to implement the boundary condition for a fixed solid wall in DUGKS is very similar to that in LBM, except that it is done at the cell interface nodes [32]. For moving solid-fluid interface, the immersed boundary method described above is typically used, see, for example, the study of Tao et al. [88] for particle-laden flows.

5.4.5 Remarks

Table 5.1: Comparison of LBM and DUGKS.

	LBM	DUGKS
Basic features	A finite-difference method along the characteristic line	A coupled finite-volume approach
Discrete velocity set	More limited due to tight coupling with the space grid	Uncoupled from the space grid, more flexibility
Mesh	Typically uniform mesh	Nonuniform / unstructured mesh allowed
Coding	Simple, only collision & streaming	More involved due to the computation of interface fluxes
Numerical stability	Less stable	More stable
Order of accuracy	Second order	Second order
Numerical dissipation	Minimal	Slightly larger than LBM due to reconstructions at the cell interface
Comput. efficiency	High	Not as high as LBM

Before ending this section, several remarks are in order. First, we compare LBM and DUGKS in Table 5.1. In general, they are comparable in terms of accuracy. LBM has some advantages over DUGKS in terms of computational efficiency, accuracy and coding simplicity, while DUGKS has been shown to be better in terms of numerical stability, mesh choice, and choice of particle velocity set. LBM is a relatively more mature approach, while DUGKS can be more easily extended to compressible and thermal flows.

Second, we compare briefly the interpolated bounce-back (IBB) scheme IBB and the immersed boundary method (IBM) for handling moving fluid-solid interface, in the context of mesoscopic methods. A direct comparison was made recently by Peng et al. [67, 66]. Consistent with the observations and remarks in the present § 5.2.3, these authors show that IBM typically yields first-order accuracy locally when the regularized delta-function is employed to interpolate velocity from the Eulerian to Lagrangian mesh, and the resulting boundary force back to the Eulerian mesh. This first order in accuracy for IBM is observed for both the local velocity and hydrodynamic force/torque. Another problem of immersed boundary methods is that the local stress within the diffused fluid-solid interface tends to be significantly underestimated, which can significantly affect the accuracy of computed viscous dissipation rate at the solid-fluid interfaces. On the other hand, the interpolated bounce-back generally possesses a second-order accuracy for velocity, hydrodynamic force/torque, and local stress field. The main disadvantage of the interpolated bounce-back schemes is its higher level of fluctuations in the calculated hydrodynamic force/torque when a solid object moves across the grid lines. Nevertheless, Peng et al. [66] show that, when a sufficient grid resolution is used, the two methods are able to provide accurate results for most of turbulent statistics in both the carrier and dispersed phases in turbulent particle-laden flow simulations.

Finally, we wish to point out that handling accurately the hydrodynamic boundary conditions in

mesoscopic methods remains an active area of research, particularly for moving solid-fluid interfaces in a turbulent flow. Issues such as Galilean invariance, pressure noises, and thermal boundary conditions are not fully resolved. While mesoscopic methods enjoy linear parallel scalability, the criterion for their numerical stability is not as well established as the traditional NSF solvers.

5.5 Reference data-sets

Since efficient algorithms for PR-DNS are non-boundary-conforming in nature, their thorough validation is primordial. However, it is not trivial to design meaningful test cases which involve the full non-linearity of the Navier-Stokes equations, coupled to rigid body motion, suitable for convergence studies. Even after a given algorithm has been fully validated in the general sense, there always remains the task of calibrating the spatio-temporal resolution to be employed in a given simulation. For this purpose high-fidelity reference data involving a three-dimensional flow field is extremely useful.

One way of generating such benchmark data is through boundary-conforming simulations, preferably using a high-order method. In this spirit the spectral-element method, with a particle-attached grid and strong coupling between the fluid and solid motion, provides excellent reference data. In the following we are discussing one such data-set in an unbounded system. Other high-fidelity data-sets featuring wall-bounded shear flows have been described in [116, 117, 119, 118].

5.5.1 Single particle settling in unbounded ambient fluid

The motion of a single particle settling in unbounded ambient flow already features a rich set of dynamics [16], where some regimes of motion exist only in a relatively narrow range of the parameter space, and therefore single-particle settling constitutes a stringent test of the numerics. Here we focus on a single parameter point which has been proposed as one of the benchmarks in [97]: an isolated sphere of density ratio $\rho_p/\rho_f = 1.5$ is settling at a Galileo number $Ga = 178.46$, which corresponds to the steady oblique regime of motion, induced by a double-threaded, off-center wake (cf. visualization in figure 5.4). The Galileo number $Ga = u_g d_p / \nu_f$ can be thought of as a particle Reynolds number computed with the a priori known gravitational velocity scale $u_g = ((\rho_p/\rho_f - 1)d_p|\mathbf{g}|)^{1/2}$ (where \mathbf{g} is the gravitational acceleration). Note that, after possible initial transients, the particle motion and the flow field are steady in a frame of reference attached to the particle in this regime, and this is the frame chosen in the reference computations performed with the method proposed in [24, 39]. In the lab-frame, however, which is chosen when performing validation tests with a PR-DNS method, the solution is unsteady. Therefore, the capability of the algorithms to capture the relative motion of an immersed body with respect to the fixed grid can be evaluated.

Figure 5.4 shows that the oblique regime is captured with non-conforming methods on a fixed grid when $\mathcal{O}(10)$ grid points per particle diameter are used. It can also be seen that the amplitude of the recirculation region is reasonably well reproduced with $d_p/\Delta x = 24$ when using a standard immersed boundary method [97]. The improvement of the prediction of the flow field around the particle due to refinement yields a corresponding improvement of the predicted hydrodynamic force, and hence of the computed particle velocity, as can be seen in figure 5.4(d). In the figure we have included the Lattice-Boltzmann-based results of Rettinger & Rde [73], which are of similar quality as the IBM results at comparable spatial and temporal resolutions. Unfortunately, no direct comparison of the two approaches with respect to computational cost is available. Note that the two non-conforming methods appear to converge to slightly different values of the particle-related quantities than the reference data (e.g. the horizontal velocity shown in figure 5.4d, and similarly for the vertical component

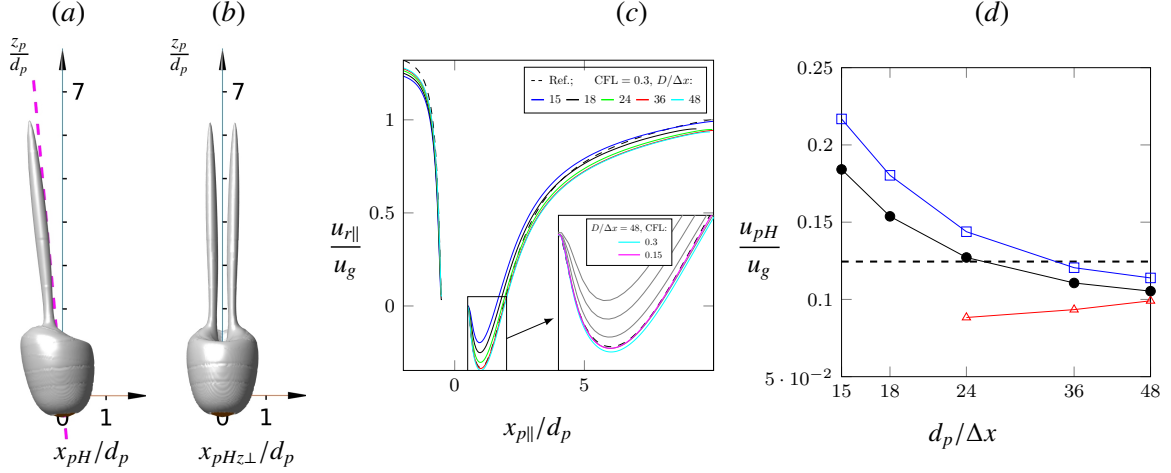


Figure 5.4: Flow around a settling sphere in the regime of steady oblique motion ($Ga = 178.46$, $\rho_p/\rho_f = 1.5$) with gravity acting in the negative z direction. (a) Lateral and (b) frontal view of the spectral-element reference solution [97] (their case “BL”), showing the double-threaded vortex structure (second invariant of the velocity gradient tensor, $\lambda_2 = -0.015u_g^2/d_p^2$, [40]). (c) Streamwise velocity component of the relative velocity, $u_{r\parallel}$, along a line parallel to the trajectory of the particle passing through its centroid (cf. the dashed magenta line in panel a). Solid lines correspond to IBM computations with different particle resolutions $d_p/\Delta x$ indicated by colors; the dashed line shows the reference spectral-element solution; the inset shows a close-up of the recirculation region, and includes a reduction of the time step. (d) The horizontal particle velocity magnitude u_{pH} as computed with different resolutions (lines with symbols), compared to the reference data from the spectral-element simulation (horizontal dashed line). —●— IBM method of [95], $CFL = 0.3$; —□— IBM method of [95], $CFL = 0.15$; —△— LBM computation of [73], using central linear interpolation. Note that the IBM data is not identical to that presented in [97]; it has been recomputed here with the procedure described in [61] such that the Galileo number matches the nominal value $Ga = 178.46$ exactly.

and the angular velocity, which are not shown), which can be attributed to the different lateral boundary conditions (periodic vs. zero-stress) and to the shape of the computational domain (cuboid vs. cylindrical).

Let us mention that analogous reference data for a settling oblate spheroid is available [61], where the authors also discuss the convergence properties of an immersed boundary method. % % % % %
% % %

5.6 Comparing PR-DNS methods: a difficult exercise

There exists a broad spectrum of PRS methods in the literature and readers may wonder which method to select for their own research. In the preceding sections, we elaborated on IBM, DLM and Boltzmann-based approaches, but we did not discuss many other methods such as ghost node [58], cut-cell [79] and overset grid [35] methods for the sake of conciseness. It is indeed tempting to compare the performance of these different methods and provide guidelines to readers in their selection process. However, such a comparison is not straightforward and may lead to erroneous conclusion if not conducted with care as it involves a variety of factors. In particular, computing performance is risky to compare as it deeply depends on programming. In fact, the same method implemented by two researchers in two different codes may lead to a significant performance variation simply because of implementation details. Another source of uncertainty is the test cases selected to conduct a comparison between assorted methods. For instance, a sub-set of methods may perform very well in dilute regimes but not well in dense regimes while another sub-set of methods may exhibit the reverse performance. Another issue that arises is the nature of the basic fluid flow solver. While some methods may be able to share the same fluid flow solver (i.e. the solver in the absence of suspended particles) such as, e.g., direct forcing/IB and DLM/FD, other methods are inextricably bound to the basic fluid flow solver such as, e.g., LBM. While a comparison of PR-DNS methods will inevitably remain hazardous if not carried out extremely thoroughly, any research group that would want to attempt such a comparison should rely on the following metrics:

- The order of spatial and temporal accuracy of the method.
- The magnitude of the spatial error as a function of the grid size. Indeed, a method may be of low order, but the prefactor of the error may be very small, thus still rendering the method effective. The same applies to the temporal error.
- The scalability on an increasing number of processes
- The absolute computing speed measured in terms of number of cells resolved per process per time step per second.

PR-DNS methods may also be compared at a more conceptual level through their design properties:

- Is the method conservative or non-conservative ?
- Is the method easily extendable to adaptive mesh refinement ?
- Does the method require hydrodynamic radius calibration and consequently does the method easily apply to non-spherical shapes ?

But then these properties should again be put to the test to assess whether some presumably more satisfactory properties (e.g. a conservative method is admittedly more suitable than a non-conservative method) lead to quantifiable differences in the data sets and, therefore, to substantially different conclusions on the flow dynamics when these data sets are analyzed. This is a daunting task that to the best of the authors' knowledge has not been addressed in detail by any previous study.

5.7 Conclusion and outlook

In the present chapter we have outlined several approaches for performing particle-resolved DNS in an efficient manner. This can be achieved with a non-conforming grid which does not need to be adapted to the evolving fluid-particle interface. Instead, the appropriate interface condition (i.e. no-slip) is typically imposed by means of source terms (IBM, cf. § 5.2), or through Lagrange multipliers (DLM, cf. § 5.3) — or possibly with the aid of one of a number of alternative techniques which have been omitted here for conciseness (e.g. sharp interface method, penalization method, overset grids). It was also shown that the choice of the basic fluid solver is not crucial to the success of PR-DNS, and that a wide variety of discretizations have been successfully employed in the past.

Numerical methods for PR-DNS have now reached a certain level of maturity, which is manifested by the relatively large body of literature reporting results achieved with the aid of this technique (cf. chapter 6 in the current volume). It should also be noted that particle shapes other than spheres do not pose a fundamental challenge to the numerical method, as discussed in chapter 11. At the same time as the number of degrees of freedom which can be tackled with this approach are continuously growing, two trends can be observed.

First, an additional gain in efficiency might be achieved through the use of adaptive mesh refinement (AMR), as pioneered in the context of IBM by Roma et al. [75], and extended by other authors [99], as well as in the context of DLM/FD [81] and LBM [74, 15, 5]. Here the promise is that the benefit in flows with a wide range of scales separated in space (e.g. dilute systems with high particle Reynolds numbers) will outweigh the higher operation count inherent in the associated complex data-structures and solvers. In the future it can be expected that the AMR approach will become more commonplace as the parameter space for PR-DNS will expand.

Second, the non-conforming methods discussed here have already proven very versatile, and many additional physical processes can be added to the purely hydrodynamic problem. A brief and non-exhaustive list of added physics which have been incorporated into numerical methods similar to the ones presented in this chapter is given in the following. Heat transfer problems in the fluid domain with different boundary conditions at the fluid-solid interface can be treated along the same lines as forcing the momentum equation [62, 113, 90]. Other authors have developed approaches for treating conjugate heat transfer problems throughout the fluid and solid domains [78]. Additional forces acting on the particles, beyond those which arise due to direct solid-solid contact or due to a failure to resolve lubrication (cf. chapter 11), can be integrated into the PR-DNS framework in a relatively straightforward manner, e.g. short-range cohesive forces [102] and electrical charges [42]. Particle deformability can be realized in the framework of deformable shell models (applicable to the simulation of capsules) with an immersed-boundary technique as shown e.g. in [49]. Non-conforming methods for PR-DNS can equally be applied to compressible flow problems involving shock-particle interaction [9, 100]. As a final point let us comment on the potential for treating phase changes with the aid of the numerical approaches discussed in the present chapter. Here the challenge lies in resolving the subtle and tightly coupled mechanical and thermal balances at the freely-evolving interface. Several authors have shown that liquid-solid melting and solidification processes can be described based

on extensions of the general ideas of the methodologies presently discussed, by tracking Lagrangian marker points which are moving at the local Stefan flow velocity [38, 37]. Other authors have resorted to a description of the interface properties based on a (Cahn-Hilliard) phase-field model, coupled to immersed-boundary-type discretizations [57]. This short glimpse into added physical effects suggests that the potential for tackling more realistic problems with the aid of the PR-DNS approach in the future is enormous. It appears therefore safe to say that we will see a growing number of applications of this technique to a broader range of systems relevant to problems found in technical devices and natural environments.

Acknowledgements: This work has received financial support from the Deutsche Forschungsgemeinschaft (DFG, German Research Foundation) through project UH 242/11-1.

Bibliography

- [1] Akiki, G., & Balachandar, S. (2016). Immersed boundary method with non-uniform distribution of Lagrangian markers for a non-uniform Eulerian mesh. *J. Comput. Phys.*, 307, 34–59.
- [2] Allen, M., & Tildesley, D. (1987). *Computer simulations of liquids*. Oxford: Clarendon Press.
- [3] Angot, P., Bruneau, C.-H., & Fabrie, P. (1999). A penalization method to take into account obstacles in incompressible viscous flows. *Num. Math.*, 81, 497–520.
- [4] Bao, Y., Donev, A., Griffith, B., McQueen, D., & Peskin, C. (2017). An immersed boundary method with divergence-free velocity interpolation and force spreading. *J. Comput. Phys.*, 347, 183–206.
- [5] Bauer, M., Eibl, S., Godenschwager, C., Kohl, N., Kuron, M., Rettinger, C., Schornbaum, F., Schwarzmeier, C., Thönnies, D., Köstler, H., & Rude, U. (2020). waLBerla: A block-structured high-performance framework for multiphysics simulations. *Computers & Mathematics with Applications*, 81, 478–501.
- [6] Beyer, B., & LeVeque, R. (1992). Analysis of a one-dimensional model for the immersed boundary method. *SIAM Journal on Numerical Analysis*, 29(2), 332–364.
- [7] Bhatnagar, P., Gross, E., & Krook, M. (1954). A model for collision processes in gases. i: small amplitude processes in charged and neutral one-component system. *Phys. Rev.*, 94, 511–525.
- [8] Bouzidi, M., Firdaouss, M., & Lallemand, P. (2001). Momentum transfer of a boltzmann-lattice fluid with boundaries. *Physics of fluids*, 13(11), 3452–3459.
- [9] Brehm, C., Hader, C., & Fasel, H. (2015). A locally stabilized immersed boundary method for the compressible Navier–Stokes equations. *J. Comput. Phys.*, 295, 475 – 504.
- [10] Breugem, W. (2012). A second-order accurate immersed boundary method for fully resolved simulations of particle-laden flows. *J. Comput. Phys.*, 231(13), 4469–4498.
- [11] Burton, T., & Eaton, J. (2002). Analysis of a fractional-step method on overset grids. *J. Comput. Physics*, 177(2), 336 – 364.
- [12] Chen, S., & Doolen, G. (1998). Lattice boltzmann method for fluid flows. *Annu. Rev. Fluid Mech.*, 30, 329–364.
- [13] Chen, T., Wang, L.-P., Lai, J., & Chen, S. (2021). Inverse design of mesoscopic models for compressible flow using the chapman-enskog analysis. *Advances in Aerodynamics*, 3(1), 1–25.
- [14] Derksen, J., & Van den Akker, H. (1999). Large eddy simulations on the flow driven by a rushton turbine. *AIChE J.*, 45, 209–221.

- [15] Eitel-Amor, G., Meinke, M., & Schröder, W. (2013). A lattice-Boltzmann method with hierarchically refined meshes. *Computers & Fluids*, *75*, 127–139.
- [16] Ern, P., Risso, F., Fabre, D., & Magnaudet, J. (2012). Wake-induced oscillatory paths of bodies freely rising or falling in fluids. *Ann. Rev. Fluid Mech.*, *44*, 97–121.
- [17] Esteghamatian, A., Hammouti, A., Lance, M., & Wachs, A. (2017). Particle resolved simulations of liquid/solid and gas/solid fluidized beds. *Physics of Fluids*, *29*(3), 033302.
- [18] Fadlun, E., Verzicco, R., Orlandi, P., & Mohd-Yusof, J. (2000). Combined immersed-boundary finite-difference methods for three-dimensional complex flow simulations. *J. Comput. Phys.*, *161*, 35–60.
- [19] Feng, Z., & Michaelides, E. (2004). The immersed boundary-lattice boltzmann method for solving fluid-particles interaction problems. *Comp. Phys*, *195*, 602–628.
- [20] Feng, Z., & Michaelides, E. (2009). Robust treatment of no-slip boundary condition and velocity updating for the lattice-boltzmann simulation of particulate flows. *Comput. Fluids*, *38*, 370–381.
- [21] Ferziger, J., & Peric, M. (2002). *Computational methods for fluid dynamics*. Springer.
- [22] Frenkel, D., & Smit, B. (2002). *Understanding molecular simulation*. Academic Press.
- [23] Gallier, S., Lemaire, E., Lobry, L., & Peters, F. (2014). A fictitious domain approach for the simulation of dense suspensions. *Journal of Computational Physics*, *256*, 367–387.
- [24] Ghidersa, B., & Dušek, J. (2000). Breaking of axisymmetry and onset of unsteadiness in the wake of a sphere. *J. Fluid Mech.*, *423*, 33–69.
- [25] Glowinski, R., Pan, T., Hesla, T., & Joseph, D. (1999). A distributed Lagrange multiplier/fictitious domain method for particulate flows. *International Journal of Multiphase Flow*, *25*(5), 755–794.
- [26] Glowinski, R., Pan, T., Hesla, T., Joseph, D., & Periaux, J. (1999). A distributed Lagrange multiplier/fictitious domain method for flows around moving rigid bodies: application to particulate flow. *International Journal for Numerical Methods in Fluids*, *30*(8), 1043–1066.
- [27] Glowinski, R., Pan, T., Hesla, T., Joseph, D., & Periaux, J. (2000). A distributed Lagrange multiplier/fictitious domain method for the simulation of flow around moving rigid bodies: application to particulate flow. *Computer Methods in Applied Mechanics and Engineering*, *184*(2-4), 241–267.
- [28] Glowinski, R., Pan, T., Hesla, T., Joseph, D., & Periaux, J. (2001). A fictitious domain approach to the direct numerical simulation of incompressible viscous flow past moving rigid bodies: application to particulate flow. *Journal of Computational Physics*, *169*(2), 363–426.
- [29] Goldstein, D., Handler, R., & Sirovich, L. (1993). Modeling a no-slip boundary with an external force field. *J. Comput. Phys.*, *105*, 354–366.
- [30] Gsell, S., & Favier, J. (2021). Direct-forcing immersed-boundary method: A simple correction preventing boundary slip error. *J. Comput. Phys.*, *435*, 110265.

- [31] Guo, Z., Wang, R., & Xu, K. (2015). Discrete unified gas kinetic scheme for all knudsen number flows. ii. thermal compressible case. *Physical Review E*, 91(3), 033313.
- [32] Guo, Z., Xu, K., & Wang, R. (2013). Discrete unified gas kinetic scheme for all knudsen number flows: Low-speed isothermal case. *Physical Review E*, 88(3), 033305.
- [33] Guo, Z., Zheng, C., & Shi, B. (2002). Discrete lattice effects on the forcing term in the lattice boltzmann method. *Physical review E*, 65(4), 046308.
- [34] Haeri, S., & Shrimpton, J. (2012). On the application of immersed boundary, fictitious domain and body-conformal mesh methods to many particle multiphase flows. *Int. J. Multiphase Flow*, 40, 38 – 55.
- [35] Henshaw, W., & Schwendemann, D. (2008). Parallel computation of three-dimensional flows using overlapping grids with adaptive mesh refinement. *J. Comput. Phys.*, 227, 7469–7502.
- [36] Hu, H., Patankar, N., & Zhu, N. (2001). Direct numerical simulation of fluid-solid systems using the arbitrary Lagrangian Eulerian technique. *J. Comput. Phys.*, 169, 427–462.
- [37] Huang, J., Shelley, M., & Stein, D. (2021). A stable and accurate scheme for solving the Stefan problem coupled with natural convection using the immersed boundary smooth extension method. *J. Comput. Phys.*, 432, 110162.
- [38] Huang, R., & Wu, H. (2014). An immersed boundary-thermal lattice Boltzmann method for solid–liquid phase change. *J. Comput. Phys.*, 277, 305–319.
- [39] Jenny, M., & Dušek, J. (2004). Efficient numerical method for the direct numerical simulation of the flow past a single light moving spherical body in transitional regimes. *J. Comput. Phys.*, 194, 215–232.
- [40] Jeong, J., & Hussain, F. (1995). On the identification of a vortex. *J. Fluid Mech.*, 285, 69–94.
- [41] Johnson, A., & Tezduyar, T. (1999). Advanced mesh generation and update methods for 3d flow simulations. *Comput. Mech.*, 23, 130–143.
- [42] Kang, S. (2013). Direct simulations on the electrophoretic motion of multiple charged particles using an immersed boundary method. *Comput. & Fluids*, 73, 10–23.
- [43] Kempe, T., & Fröhlich, J. (2012). An improved immersed boundary method with direct forcing for the simulation of particle laden flows. *J. Comput. Phys.*, 231(9), 3663–3684.
- [44] Kidanemariam, A., & Uhlmann, M. (2017). Formation of sediment patterns in channel flow: minimal unstable systems and their temporal evolution. *J. Fluid Mech.*, 818, 716–743.
- [45] Kim, D., & Choi, H. (2006). Immersed boundary method for flow around an arbitrarily moving body. *J. Comput. Phys.*, 212, 662–680.
- [46] Kim, J., Kim, D., & Choi, H. (2001). An immersed-boundary finite-volume method for simulations of flow in complex geometries. *J. Comput. Phys.*, 171, 132–150.
- [47] Kim, W., & Choi, H. (2019). Immersed boundary methods for fluid-structure interaction: A review. *Int. J. Heat Fluid Flow*, 75, 301 – 309.

- [48] Kolomenskiy, D., & Schneider, K. (2009). A Fourier spectral method for the Navier–Stokes equations with volume penalization for moving solid obstacles. *J. Comput. Phys.*, [228\(16\)](#), 5687 – 5709.
- [49] Krüger, T., Varnik, F., & Raabe, D. (2011). Efficient and accurate simulations of deformable particles immersed in a fluid using a combined immersed boundary lattice Boltzmann finite element method. *Comput. Math. Appl.*, [61\(12\)](#), 3485–3505.
- [50] Ladd, A. (1994). Numerical simulations of particulate suspensions via a discretized boltzmann equation. part 1. theoretical foundation. *J. Fluid Mech.*, [271](#), 285–309.
- [51] Ladd, A. (1994). Numerical simulations of particulate suspensions via a discretized boltzmann equation. part 2. numerical results. *J. Fluid Mech.*, [271](#), 311–339.
- [52] Leopardi, P. (2006). A partition of the unit sphere into regions of equal area and small diameter. *Electr. Trans. Num. Analysis*, [25](#), 309–327.
- [53] Lima E Silva, A., Silveira-Neto, A., & Damasceno, J. (2003). Numerical simulation of two-dimensional flows over a circular cylinder using the immersed boundary method. *Journal of Computational Physics*, [189\(2\)](#), 351–370.
- [54] Luo, K., Wang, Z., Fan, J., & Cen, K. (2007). Full-scale solutions to particle-laden flows: Multidirect forcing and immersed boundary method. *Phys. Rev. E*, [76](#), 066709.
- [55] Luo, K., Wang, Z., Tan, J., & Fan, J. (2019). An improved direct-forcing immersed boundary method with inward retraction of Lagrangian points for simulation of particle-laden flows. *J. Comput. Phys.*, [376](#), 210 – 227.
- [56] Mark, A., & van Wachem, B. (2008). Derivation and validation of a novel implicit second-order accurate immersed boundary method. *J. Comput. Phys.*, [227\(13\)](#), 6660–6680.
- [57] Meng, S., Zhang, A., Guo, Z., & Wang, Q. (2020). Phase-field-lattice Boltzmann simulation of dendrite motion using an immersed boundary method. *Comput. Mat. Sci.*, [184](#), 109784.
- [58] Mittal, R., Dong, H., Bozkurttas, M., Najjar, F., Vargas, A., & von Loebbecke, A. (2008). A versatile sharp interface immersed boundary method for incompressible flows with complex boundaries. *J. Comput. Phys.*, [227\(10\)](#), 4825–4852.
- [59] Mittal, R., & Iaccarino, G. (2005). Immersed boundary methods. *Annu. Rev. Fluid Mech.*, [37\(1\)](#), 239–261.
- [60] Mohd-Yusof, J. (1997). Combined immersed-boundary/B-spline methods for simulations of flow in complex geometries. *CTR Res. Briefs*, (pp. 317–327).
- [61] Moriche, M., Uhlmann, M., & Dušek, J. (2021). A single oblate spheroid settling in unbounded ambient fluid: a benchmark for simulations in steady and unsteady wake regimes. *Int. J. Multiphase Flow*, [1346](#), 103519.
- [62] Pacheco, J., Pacheco-Vega, A., Rodic, T., & Peck, R. (2005). Numerical simulations of heat transfer and fluid flow problems using an immersed-boundary finite-volume method on non-staggered grids. *Num. Heat Transf., Part B*, [48](#), 1–24.

- [63] Pan, Y., & Banerjee, S. (1997). Numerical investigation of the effects of large particles on wall-turbulence. *Phys. Fluids*, 9(12), 3786–3807.
- [64] Patankar, N. (2001). A formulation for fast computations of rigid particulate flows. *CTR Res. Briefs*, (pp. 185–196).
- [65] Patankar, N., Singh, P., Joseph, D., Glowinski, R., & Pan, T. (2000). A new formulation of the distributed Lagrange multiplier/fictitious domain method for particulate flows. *International Journal of Multiphase Flow*, 26(9), 1509–1524.
- [66] Peng, C., Ayala, O. M., de Motta, B. J., & Wang, L.-P. (2019). A comparative study of immersed boundary method and interpolated bounce-back scheme for no-slip boundary treatment in the lattice boltzmann method: Part ii, turbulent flows. *Comput. Fluids*, 192, 104251.
- [67] Peng, C., Ayala, O. M., & Wang, L.-P. (2019). A comparative study of immersed boundary method and interpolated bounce-back scheme for no-slip boundary treatment in the lattice boltzmann method: Part i, laminar flows. *Computers & Fluids*, 192, 104233.
- [68] Peskin, C. (1972). Flow patterns around heart valves: A digital computer method for solving the equations of motion. Ph.D. thesis, Albert Einstein College of Medicine of Yeshiva University, New York, USA.
- [69] Peskin, C. (1972). Flow patterns around heart valves: A numerical method. *J. Comput. Phys.*, 10(2), 252–271.
- [70] Peskin, C. (2002). The immersed boundary method. *Acta Numerica*, 11, 479–517.
- [71] Pinelli, A., Naqavi, I., Piomelli, U., & Favier, J. (2010). Immersed-boundary methods for general finite-difference and finite-volume Navier–Stokes solvers. *J. Comput. Phys.*, 229(24), 9073–9091.
- [72] Rahmani, M., & Wachs, A. (2014). Free falling and rising of spherical and angular particles. *Physics of Fluids*, 26, 083301.
- [73] Rettinger, C., & Rde, U. (2017). A comparative study of fluid-particle coupling methods for fully resolved lattice Boltzmann simulations. *Comput. & Fluids*, 154, 74–89.
- [74] Rohde, M., Kandhai, D., Derksen, J. J., & Van den Akker, H. E. A. (2006). A generic, mass conservative local grid refinement technique for lattice-Boltzmann schemes. *International Journal for Numerical Methods in Fluids*, 51(4), 439–468.
- [75] Roma, A., Peskin, C., & Berger, M. (1999). An adaptive version of the immersed boundary method. *J. Comput. Phys.*, 153, 509–534.
- [76] Saff, E., & Kuijlaars, A. (1997). Distributing many points on a sphere. *Math. Intelligencer*, 19(1), 5–11.
- [77] Saiki, E., & Biringen, S. (1996). Numerical simulation of a cylinder in uniform flow: Application of a virtual boundary method. *J. Comput. Phys.*, 123, 450–465.
- [78] Sato, N., Takeuchi, S., Kajishima, T., Inagaki, M., & Horinouchi, N. (2016). A consistent direct discretization scheme on Cartesian grids for convective and conjugate heat transfer. *J. Comput. Phys.*, 321, 76 – 104.

- [79] Schneiders, L., Günther, C., Meinke, M., & Schröder, W. (2016). An efficient conservative cut-cell method for rigid bodies interacting with viscous compressible flows. *J. Comput. Phys.*, 311, 62–86.
- [80] Schwarz, S., Kempe, T., & Fröhlich, J. (2015). A temporal discretization scheme to compute the motion of light particles in viscous flows by an immersed boundary method. *J. Comput. Phys.*, 281, 591–613.
- [81] Selcuk, C., Ghigo, A. R., Popinet, S., & Wachs, A. (2021). A fictitious domain method with distributed Lagrange multipliers on adaptive quad/octrees for the direct numerical simulation of particle-laden flows. *Journal of Computational Physics*, 430, 109954.
- [82] Seyed-Ahmadi, A., & Wachs, A. (2019). Dynamics and wakes of freely settling and rising cubes. *Physical Review Fluids*, 4(7), 074304.
- [83] Shan, X., Yuan, X.-F., & Chen, H. (2006). Kinetic theory representation of hydrodynamics: a way beyond the navier–stokes equation. *Journal of Fluid Mechanics*, 550, 413–441.
- [84] Sharma, N., & Patankar, N. (2005). A fast computation technique for the direct numerical simulation of rigid particulate flows. *J. Comput. Phys.*, 205(2), 439–457.
- [85] Shu, C., Wang, Y., Teo, C., & Wu, J. (2014). Development of lattice boltzmann flux solver for simulation of incompressible flows. *Advances in Applied Mathematics and Mechanics*, 6(4), 436–460.
- [86] Sotiropoulos, F., & Yang, X. (2014). Immersed boundary methods for simulating fluid–structure interaction. *Progress Aerospace Sci.*, 65, 1 – 21.
- [87] Taira, K., & Colonius, T. (2007). The immersed boundary method: A projection approach. *J. Comput. Phys.*, 225(2), 2118–2137.
- [88] Tao, S., Zhang, H., Guo, Z., & Wang, L.-P. (2018). A combined immersed boundary and discrete unified gas kinetic scheme for particle–fluid flows. *Journal of Computational Physics*, 375, 498–518.
- [89] Tavanashad, V., & Subramaniam, S. (2020). Fully resolved simulation of dense suspensions of freely evolving buoyant particles using an improved immersed boundary method. *International Journal of Multiphase Flow*, 132, 103396.
- [90] Tavassoli, H., Kriebitzsch, S., van der Hoef, M., Peters, E., & Kuipers, J. (2013). Direct numerical simulation of particulate flow with heat transfer. *Int. J. Multiphase Flow*, 57, 29 – 37.
- [91] ten Cate, A., Derksen, J., Portela, L., & van den Akker, H. (1994). Fully resolved simulations of colliding spheres in forces isotropic turbulence. *J. Fluid Mech.*, 519, 233–271.
- [92] Tennetti, S., Garg, R., & Subramaniam, S. (2011). Drag law for monodisperse gas-solid systems using particle-resolved direct numerical simulation of flow past fixed assemblies of spheres. *Int. J. Multiphase Flow*, 37, 1072–1092.
- [93] Tschisgale, S., Kempe, T., & Fröhlich, J. (2017). A non-iterative immersed boundary method for spherical particles of arbitrary density ratio. *J. Comput. Phys.*, 339, 432–452.

- [94] Udaykumar, H., Mittal, R., Rampunggoon, P., & Khanna, A. (2001). A sharp interface Cartesian grid method for simulating flows with complex moving boundaries. *J. Comput. Phys.*, [174\(1\)](#), 345 – 380.
- [95] Uhlmann, M. (2005). An immersed boundary method with direct forcing for the simulation of particulate flows. *J. Comput. Phys.*, [209\(2\)](#), 448–476.
- [96] Uhlmann, M. (2005). An improved fluid-solid coupling method for DNS of particulate flow on a fixed mesh. In M. Sommerfeld (Ed.) *Proc. 11th Workshop Two-Phase Flow Predictions*. Merseburg, Germany: Universität Halle. ISBN 3-86010-767-4.
- [97] Uhlmann, M., & Dušek, J. (2014). The motion of a single heavy sphere in ambient fluid: a benchmark for interface-resolved particulate flow simulations with significant relative velocities. *Int. J. Multiphase Flow*, [59](#), 221–243.
- [98] Vanella, M., & Balaras, E. (2009). A moving-least-squares reconstruction for embedded-boundary formulations. *J. Comput. Phys.*, [228\(18\)](#), 6617–6628.
- [99] Vanella, M., Posa, A., & Balaras, E. (2014). Adaptive mesh refinement for immersed boundary methods. *J. Fluids Eng.*, [136\(4\)](#).
- [100] Vanna, F. D., Picano, F., & Benini, E. (2020). A sharp-interface immersed boundary method for moving objects in compressible viscous flows. *Comput. & Fluids*, [201](#), 104415.
- [101] Veeramani, C., Mineev, P., & Nandakumar, K. (2007). A fictitious domain formulation for flows with rigid particles: A non-Lagrange multiplier version. *Journal of Computational Physics*, [224\(2\)](#), 867–879.
- [102] Vowinckel, B., Withers, J., Luzzatto-Fegiz, P., & Meiburg, E. (2019). Settling of cohesive sediment: particle-resolved simulations. *J. Fluid Mech.*, [858](#), 5–44.
- [103] Wachs, A. (2019). Particle-scale computational approaches to model dry and saturated granular flows of non-Brownian, non-cohesive, and non-spherical rigid bodies. *Acta Mech.*, [230](#), 1919–1980.
- [104] Wachs, A., Hammouti, A., Vinay, G., & Rahmani, M. (2015). Accuracy of Finite Volume/Staggered Grid Distributed Lagrange Multiplier/Fictitious Domain simulations of particulate flows. *Computers & Fluids*, [115](#), 154–172.
- [105] Wen, X., Wang, L.-P., & Guo, Z. (2021). Designing a consistent implementation of the discrete unified gas-kinetic scheme for the simulation of three-dimensional compressible natural convection. *Physics of Fluids*, [33\(4\)](#), 046101.
- [106] Wen, X., Wang, L.-P., Guo, Z., & Shen, J. (2021). An improved discrete unified gas kinetic scheme for simulating compressible natural convection flows. *Journal of Computational Physics: X*, [11](#), 100088.
- [107] Xu, K. (2001). A gas-kinetic bgk scheme for the navier–stokes equations and its connection with artificial dissipation and godunov method. *Journal of Computational Physics*, [171\(1\)](#), 289–335.

- [108] Yiantsios, S. (2012). On the distributed Lagrange multiplier/fictitious domain method for rigid-particle-laden flows: a proposition for an alternative formulation of the Lagrange multipliers. International Journal for Numerical Methods in Fluids, *70*, 1027–1047.
- [109] Yu, D., Mei, R., Luo, L.-S., & Shyy, W. (2003). Viscous flow computations with the method of lattice boltzmann equation. Progress in Aerospace Sciences, *39*(5), 329–367.
- [110] Yu, Z., Phan-Thien, N., Fan, Y., & Tanner, R. (2002). Viscoelastic mobility problem of a system of particles. Journal of Non-Newtonian Fluid Mechanics, *104*(2-3), 87–124.
- [111] Yu, Z., Phan-Thien, N., & Tanner, R. (2004). Dynamic simulation of sphere motion in a vertical tube. Journal of Fluid Mechanics, *518*, 61–93.
- [112] Yu, Z., & Shao, X. (2007). A direct-forcing fictitious domain method for particulate flows. Journal of Computational Physics, *227*(1), 292–314.
- [113] Yu, Z., Shao, X., & Wachs, A. (2006). A fictitious domain method for particulate flows with heat transfer. Journal of Computational Physics, *217*(2), 424–452.
- [114] Yu, Z., & Wachs, A. (2007). A fictitious domain method for dynamic simulation of particle sedimentation in Bingham fluids. Journal of Non-Newtonian Fluid Mechanics, *145*(2), 78–91.
- [115] Yu, Z., Wachs, A., & Peysson, Y. (2006). Numerical simulation of particle sedimentation in shear-thinning fluids with a fictitious domain method. Journal of Non-Newtonian Fluid Mechanics, *136*(2), 126–139.
- [116] Zeng, L., Balachandar, S., & Fischer, P. (2005). Wall-induced forces on a rigid sphere at finite Reynolds numbers. J. Fluid Mech., *536*, 1–25.
- [117] Zeng, L., Balachandar, S., Fischer, P., & Najjar, F. (2008). Interactions of a stationary finite-size particle with wall-turbulence. J. Fluid Mech., *594*, 271–305.
- [118] Zeng, L., Balachandar, S., & Najjar, F. (2010). Wake response of a stationary finite-sized particle in a turbulent channel flow. Int. J. Multiphase Flow, *36*, 406–422.
- [119] Zeng, L., Najjar, F., Balachandar, S., & Fischer, P. (2009). Forces on a finite-sized particle located close to a wall in a linear shear flow. Phys. Fluids, *21*(3), 033302.
- [120] Zhang, L., Gerstenberger, A., Wang, X., & Liu, W. (2004). Immersed finite element method. Comput. Meth. Appl. Mech. Eng., *193*(21), 2051–2067.
- [121] Zhang, Z., & Prosperetti, A. (2003). A method for particle simulation. J. Appl. Mech., *70*, 64–74.
- [122] Zhou, K., & Balachandar, S. (2021). An analysis of the spatio-temporal resolution of the immersed boundary method with direct forcing. J. Comput. Phys., *424*, 109862.
- [123] Zhu, L., Wang, P., & Guo, Z. (2017). Performance evaluation of the general characteristics based off-lattice boltzmann scheme and dugks for low speed continuum flows. Journal of Computational Physics, *333*, 227–246.